Time resolved transmission electron microscopy: the structural dynamics of explosive crystallization in amorphous germanium.

Mark J. Stern

Department of Physics
McGill University
Montréal, Québec, Canada
December 2012

A thesis submitted to McGill University
in partial fulfilment of the requirements of the degree of
Master of Science

For my friends and family.

Abstract

The transmission electron microscope (TEM) is a powerful and flexible tool for the study of material structure. By incorporating a pump-probe approach in these instruments, the distinct advantages of the TEM can be exploited for the study of short lived (or rapidly time-evolving) processes in materials. This has recently been accomplished at Lawrence Livermore National Laboratory (USA), which houses a unique Dynamic Transmission Electron Microscope (DTEM). Here we demonstrate the application of this system to laser-induced crystallization dynamics in amorphous Germanium (a-Ge). During the complex process, the material undergoes several distinct modes of crystal growth that produce intricate microstructural patterns on nanosecond to ten microsecond timescales. Previous studies of this process have lacked the spatio-temporal resolution to observe the evolution of the crystal microstructure in detail. This thesis shows that Dynamic Transmission Electron Microscopy (DTEM) is uniquely well suited to study such fast, complex crystallization dynamics due to the combined 10 nm spatial and 15 ns temporal resolutions. Using DTEM, we have obtained time-resolved snap shots of the initiation and roughening of dendrites on sub-microsecond time-scales followed by a rapid transition to an unanticipated ledge-like growth mechanism that produces a layered microstructure on the several microsecond timescale. This study provides new insights into the mechanisms governing this complex crystallization process and provides a dramatic demonstration of the power of DETM for studying time-dependent material processes far from equilibrium.

Résumé

La Microscopie électronique en transmission (MET) a une capacité unique pour l'étude la structure des matériaux. En utilisant la m'ethode pompe-sonde, les avantages distinctifs de la MET peuvent être exploitée pour l'étude des processus d'une durée très courte, tels que la cristallisation des semi-conducteurs. En particulier, la cristallisation de germanium amorphe , induite par le echaufement par faiseaux laser ou éléctronique, est un sujet idéal pour l'étude MET. Au cours du processus complexe, on voit plusieurs modes distincts de croissance des cristaux qui produisent des microstructures complexes de microstructure sur l'ordre de quelques nanosecondes jusquà un dizaine des microseconds. Les efforts précédents manquent la résolution spatio-temporelle pour observer l'évolution detaillée de la structure micro et nanocrystalline. Cette thèse démontre que la microscopie électronique en transmission dynamique METD) est un outil idéal pour étudier ce processus, et possède un excellent potentiel pour l'étude de la dynamique de la cristallisation rapide et complexe. Des images de la cristallisation explosive du germanium amorphe ont été produites avec la résolution de quelques nanomètres et quelques nanosecondes. Cettes images révèlent des détails sur l'initiation et la croissance inégale du front de cristallisation, ainsi une transition rapide à un mode de croissance oscillant. Grâce à ces données nouvelles, combinées avec un modèle pour le profil de la température en fonction du temps, les conclusions perspicaces peuvent être faites au sujet de la nature des mécanismes de croissance qui controlent le processus de cristallisation complexe. Les résultats sont une démonstration spectaculaire de la capacité de l'DTEM pour étudier les processus des matériaux qui se passe pendant les intervalles courtes.

Acknowledgements

Thank you to my co-workers in both the Siwick and Kambhampati groups. Also, thanks to Heide Ibrahim, Lily Nikolova and Richard Stern, my father, for all their help and support. Finally, I cannot thank my supervisor, Brad Siwick, enough for his patience, leadership and guidance during both the research and writing processes.

Table of Contents

List of Figures

CHAPTER 1

Recent Advances in Electron Microscopy

The Transmission Electron Microscope (TEM) is an indispensable tool for materials research. Since the first TEMs were constructed in the 1930s, continuous developments in spatial resolution, sample handling, electron imaging detectors and spectrometers have widened the potential applications of the microscope. This chapter will discuss some of these recent developments in order to provide the context in which this thesis work can be understood. In particular, how the recent enhancements in spatial resolution and chemical sensitivity are now being complemented by dramatic improvements in time resolution. These developments significantly expand the capabilities of the instrument beyond the characterization of static structure to following rapid time dependent phenomena in materials.

A schematic TEM column is shown in Fig. 1–1. Conventionally, the electron beam in a TEM is emitted by a heated filament (thermionic emission) or a cold cathode subject to a strong electrostatic potential (field emission). The electrons are then accelerated down the column at voltages ranging between 100-300 kV. The beam is then focused by several magnetic lenses, which control the illumination conditions (both spot size and beam collimation). Electrons in the illuminating beam are both elastically and inelastically scattered by the specimen and can be made to produce an image or a diffraction pattern at the detector camera depending on the post-specimen aperture and lens settings. The bright field mode uses electrons in the main transmitted beam to form the image. Thicker areas of the sample, as well as crystalline areas that produce Bragg diffraction, will appear as dark regions in a bright field image. If it is more desirable to highlight these areas, switching to dark field will capture the scattered electrons; inverting the image contrast. This is useful in distinguishing small crystallites in an amorphous bulk. In diffraction mode, the electron distribution in the back focal plane of the objective lens is imaged at the detector, which can be used to determine overall crystallographic structure and other periodic features of the illuminated area of the specimen.

A conventional TEM can be used to observe dislocations, interfaces and other localized micro or nano structural details directly. In fact the TEM is unique in its ability to produce real-space images of bulk material structure with spatial resolution of less than 10 nm. Furthermore, the spatial resolution of TEM pictures can be drastically increased by using a technique, called phase contrast imaging. Electron microscopes equipped for this technique are called high resolution TEMs, and have sufficient spatial resolution to produce images of atomic columns (Fig. 1–3). The best resolution achieved to date in an electron microscope is less than an angstrom [7].

In addition to providing spatial information, inelastically scattered electrons in a TEM can be used to reveal the elemental composition of the sample. Electron probe beams smaller than 1 nm are now available in a TEM and can be used to perform analytical studies of materials structure and interfaces down to the atomic level. Interactions with both the positively charged nuclei and the negatively charged

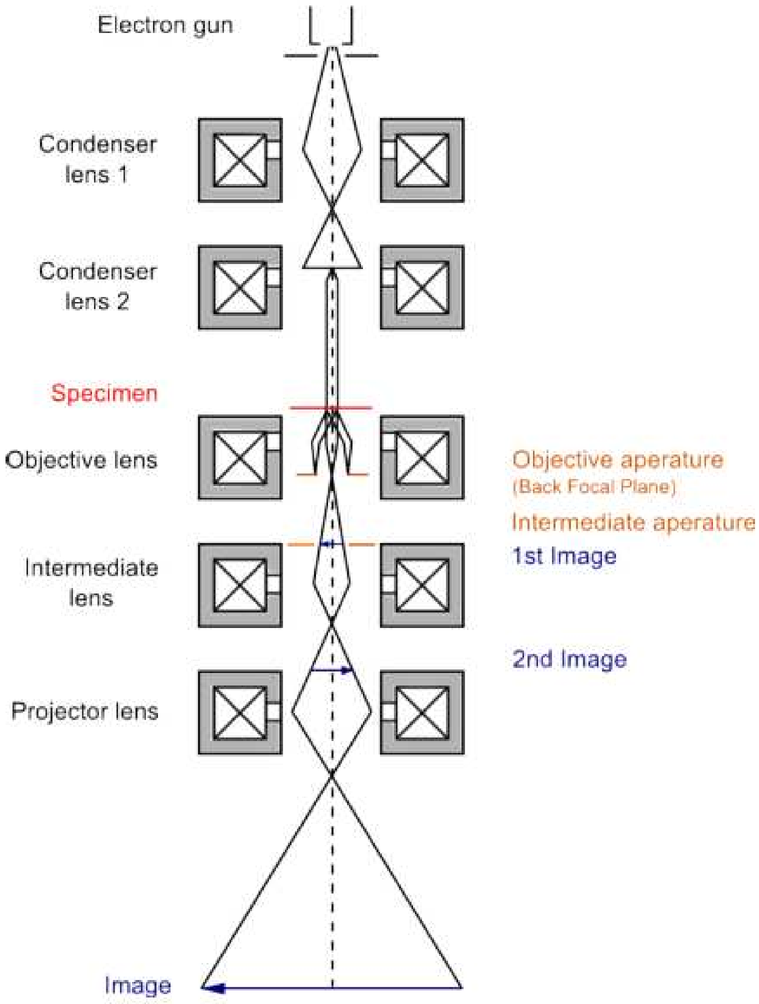

Figure 1–1: Block diagram of typical TEM.

surrounding electrons, results in various possible scattering events. Fig. 1–2 shows all possible electron scattering events interacting with a system. Energy-dispersive x-ray spectrometry (EDS) applies solid state detectors to measure x-rays emitted from the illuminated sample. The energy spectrum of these x-rays, as shown in Fig. 1–4, is compared with characteristic x-ray spectra of the chemical elements to determine chemical concentrations in the illuminated region. Electron energy-loss spectrometry (EELS) requires a post-specimen energy analyzer to determine the spectrum of the

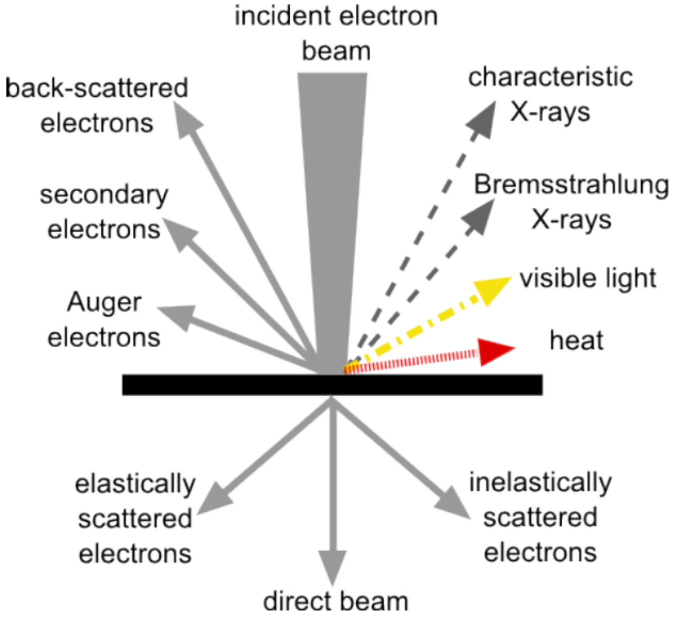

Figure 1–2: Electron scattering interactions with a thin sample.

inelastically scattered electrons, as shown in Fig. 1–5, and provides information on both plasmon excitations and core electron excitations which reveal local chemistry and structure.

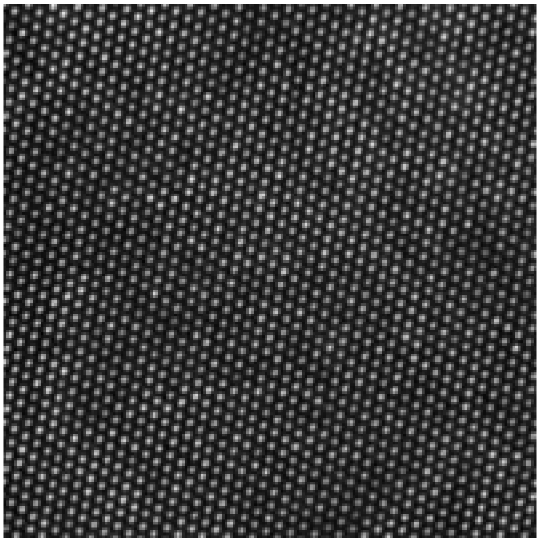

FIGURE 1–3: High resolution TEM image of Si in [110] orientation, demonstrating the effect on phase contrast imaging.

1.1 Developments in Transmission Electron Microscopy Instrumentation

In order to study a wider variety of systems, extensive efforts have been made to adapt TEM instrumentation. The major developments in TEM over the last two decades have been in several directions. i) Improvements in spatial resolution brought about by aberration corrected electron optics ii) Developments in the sensitivity and resolution of analytical electron based spectroscopies (EELS and EDS) and iii) In-situ preparation of specimen environments such as, high temperature, external magnetic/electric fields [8, 9], high vacuum [10], gaseous and liquid environments [11–15], specific load conditions [16–19], *etc.* iv) Enhancements in instrument time resolution.

Conventional electron microscopy has, historically, been resolution-limited by aberration effects. Chromatic aberration occurs due to variations in the electron energies from the source, which is often not monochromatic. Magnetic lenses do not act independent of the electron energy (or de Broglie wavelength) causing each electron

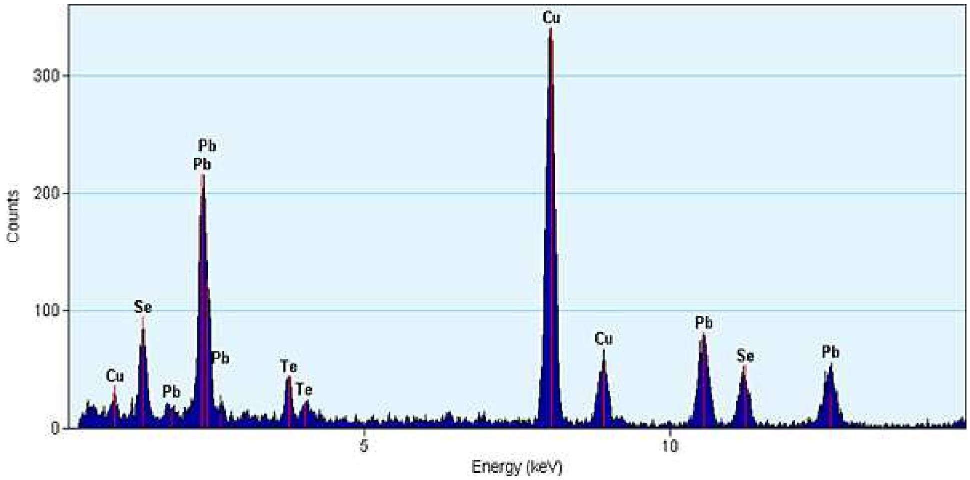

Figure 1–4: TEM EDS reveals a mixture of PbSe and PbTe nanoparticles present on carbon support film Cu grid.

energy to be focused differently, blurring the resulting image. Another common effect is due to high potential at the edge of a rotationally symmetric magnetic lens. The outer zones focus more strongly than the inner zones, which causes blurring called spherical aberration. The implementation of high quality, low aberration lenses, as well as chromatic and spherical aberration correctors have mitigated these issues and allowed the TEM to stand as a uniquely powerful tool for studying systems at or nearly at equilibrium [20].

The TEM can also be adapted to view non-equilibrium or dynamic systems, and to explore the time evolution of material structure. The simplest approach to dynamics in a TEM is by improving the readout time of the camera or detector at the end of the TEM column, using the TEM like a conventional video camera. This research direction was initiated more than 60 years ago in experiments run by Peter Hirsch [21,22]. Linear defects, called dislocations, were observed *in situ* during straining experiments of metallic foils. Combining the TEM with a film camera capable of millisecond temporal resolution allowed the motion of these dislocations to

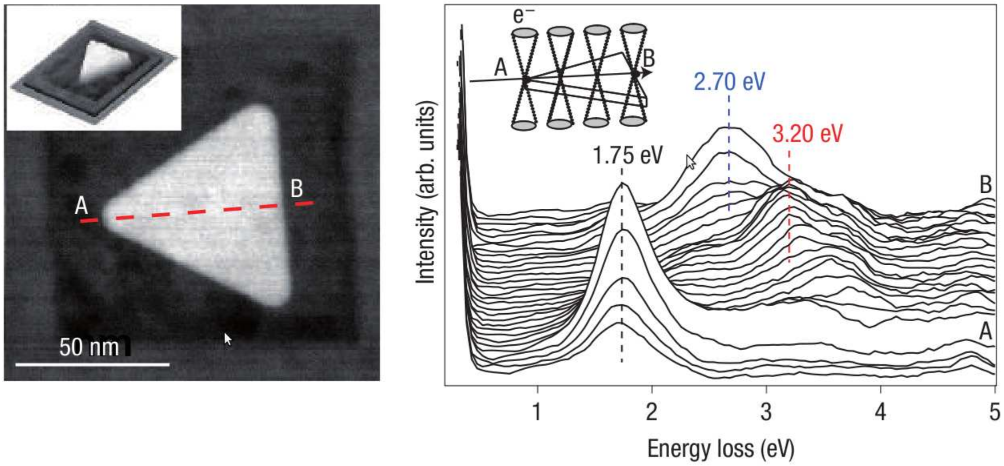

FIGURE 1–5: EELS measurements on an equilateral Ag nanoprism with 78-nm-long sides. A series of 32 successive low-loss EEL spectra acquired, in the spectrum-image mode, along an axis (A to B) of the nanoprism as illustrated in the inset. The position of the three main resonances detected along the line scan are marked by dotted lines. Reprinted with permission from [1]. Copyright 2007, Nature Publishing Group

be recorded. The results obtained supported theoretical models of dislocation structure and interaction dynamics [22]. Time resolved TEM images relate microscopic features to macroscopic behaviour. With refinements in spatio-temporal resolution, the large scale consequences of angstrom level structural dynamics can be revealed.

Observing dynamic phenomena is limited by the motion blur of their mobile features. To achieve motion blur less than 10 nm with 33 ms video rates requires the moving feature of interest to be slower than 3×10^6 m/s. This is slow compared to the characteristic speeds of many interesting systems, such as diffusional transformations [23], plastic deformation under nanoindentation [17, 24], rapid solidification and devitrification processes or shock-front propgation. Over the last 40 years, there has been great interest in improving the time resolution of TEM techniques [3, 25–31] by using pump-probe techniques.

1.2 Pump-probe Methods

The problem with continuous illumination is that the time resolution is limited by the readout speed of the camera. However, if the dynamics of interest is induced by a short laser pulse (pump pulse), it is possible to work around this limitation. The continuous illumination can then be replaced with a second short pulse (probe pulse) that contacts the sample at the same time, or just after, the arrival of the pump pulse. The resulting data will portray the dynamics at the moment of excitation and the time resolution will depend on the duration of the exposure instead of the speed of the camera. A typical pump probe setup is shown in Fig. 1–6. If ultra-short duration laser pulses are used to both photoexcite the specimen and generate (through photoemission) ultra-short electron exposure time, this approach has the potential to dramatically improve temporal resolution. This approach requires the TEM column to be equipped with this type of electron gun as well as an external optical line to pump the sample.

Traditionally, sub-microsecond dynamics in material systems, as well as chemical and biochemical reactions, have been observed with laser pump-probe techniques. Due to the growing interest in the use of electrons as probes and the advantages of TEM techniques, two approaches have been developed for high time resolution TEM imaging in pump-probe experiments. The appropriateness of each approach depends on the nature of the dynamics one is trying to observe. In the case of a unique and irreversible process, such as crystallization, one must be able to capture a TEM image *in situ* with a single exposure [2, 3, 6, 25–27, 29, 32, 33]. However, for a reversible, repeatable process, such as heating, multiple experiments can be performed in rapid succession and then averaged. This is known as the stroboscopic method [28, 30, 31, 34–40]. A modified TEM column is shown in Fig. 1–7.

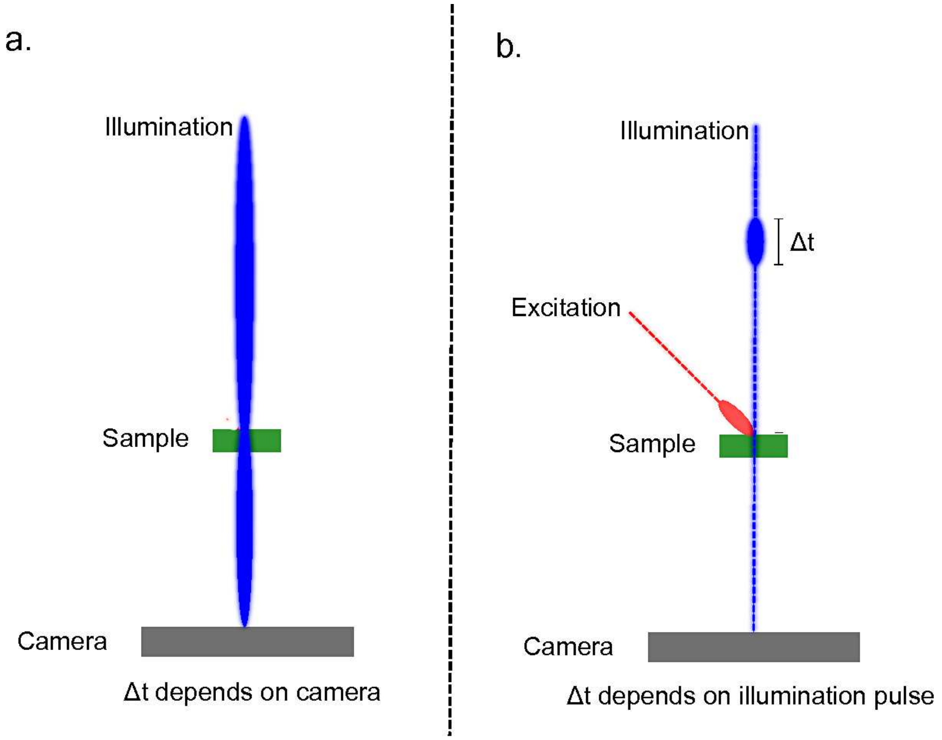

Figure 1–6: a. Continuous illumination with fast readout. b. Pump-probe with slow readout.

Whether all the electrons travel together, or individually over many repetitions, a total of about 10^8 electrons are needed to produce a reasonable image in a TEM. Under normal conditions, a TEM has only a single electron in the column at any time on average. It becomes clear that the electron bunches required for single shot instruments work under very different conditions. Heavy modifications must be made to the components in the TEM column to get the brightness required for single shot experiments [3, 41].

The stroboscopic approach also requires access to the electron source and the sample, but does not need extensive changes to the instruments in the TEM column. The exposure of 10^8 electrons is produced at a rate of approximately one electron per pulse, which results in similar electron beam conditions as in a conventional TEM.

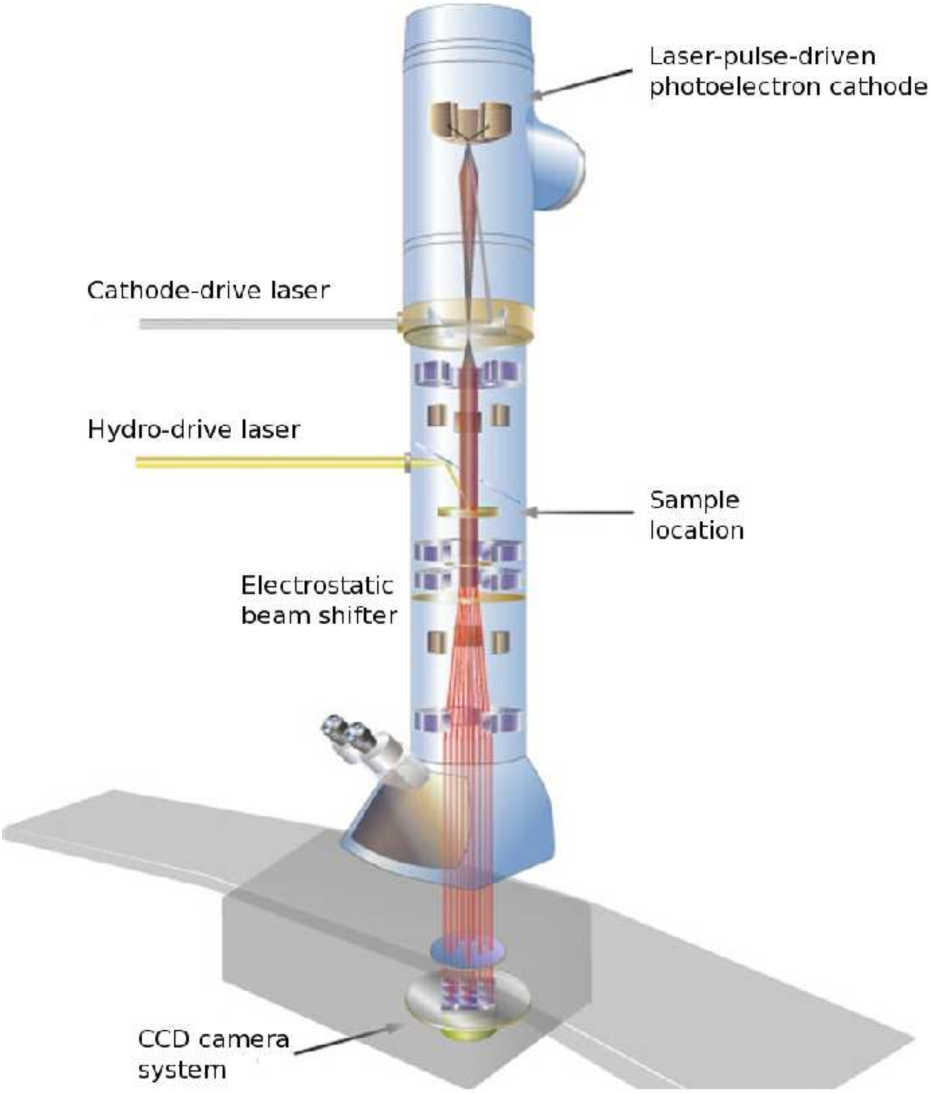

Figure 1–7: Schematic of a modified TEM for pump probe experiments. A stroboscopic instrument will use a femtosecond cathode-drive laser operating at a high repetition rate. A single shot instrument will use a nanosecond cathode-drive laser operating at a low repetition rate. Reprinted with permission from [2]. Copyright 2006, American Institute of Physics.

Thus, stroboscopic images are capable of very high spatial resolution. Zewail *et al.* at CalTech have recently employed femtosecond lasers and a field emission TEM with highenergy resolution electron energy loss spectrometer, allowing both subpicosecond timeresolved imaging and spectroscopy using the stroboscopic technique [28, 31, 42].

1.3 4D Ultrafast Electron Microscope

The stroboscopic TEM method has been pioneered in the lab of Prof. A. Zewail at CalTech and is referred as 4D ultrafast electron microscopy (4D UEM) in the literature [28, 31]. The idea behind the technique is to split the optical line of a femptosecond laser into the pump and probe pulses. The laser produces pulses at a Megahertz or higher repetition rate. The pump excites the specimen while the second optical line produces electron probe pulses via photoemission. The time between the pulses is set using a simple optical delay line. Each pulse only contains a single electron on average, eliminating space charge effects and maintaining the image resolution of the instrument when operated in continuous beam mode. The instrument was recently used to observe structural transitions in graphite films. Heating a graphitic foil with a femtosecond laser pulse is thought to cause a structural transition a few picoseconds later [35, 38, 40]. The resulting lattice expansion is too large to be caused by a thermal effect. Theoretically, this is attributed to a bonding hybridization change from sp2 graphite to sp3 diamond lasting for several picoseconds before the material relaxes. This was confirmed using femptosecond electron energy loss spectroscopy (FEELS)[48 49]. More recently, plasmon dynamics in metal nanostructures were observed [43].

The strength of this technique is its ability to illuminate subtle details of the dynamics of transient states at previously unachieved spatiotemporal resolution, allowing insight into the relationship between atomic structural changes, chemical ordering and electronic structure on timescales of less than a picosecond. However, the restriction that the 4D UEM cannot be used to study irreversible phenomena, motivates more development of the single shot technique; not many specimens will survive 10^8 pump probe cycles in a fully reversible fashion.

1.4 Dynamic Transmission Electron Microscopy

First attempts at single shot pump-probe TEM technique were pioneered by Bostanjoglo *et. al.* [44] in the 1980s. The instrument was used to study laser induced phase transitions in amorphous Ge and $\mathrm{Ge_{0,6}Te_{0,4}}$ films, with 3 ns time resolution. The design of the modern single shot instrument, known as the Dynamic Transmission Electron Microscope (DTEM), was undertaken at Lawrence Livermore National Labs (LLNL). The developments are summarized here [41,45]. A JOEL 2000FX 200 kV microscope was modified to allow a pump laser to excite the sample and to allow a laser to illuminate the cathode in order to produce the electron pulses. (Fig. 1–8). Two core improvements were made to the previous designs of the Bostanjoglo single-shot instrument. They are the laser-driven photogun and the electron optic configuration of the TEM column.

The cathode laser is an Nd:YLF (Neodymium doped yttrium lithium fluoride, $\mathrm{Nd : LiYF_4}$) laser that produces a pulsed beam with wavelength of 1053 nm and a pulse length of 70 ns. The pulse is frequency converted to the fifth harmonic (211 nm) and is then incident upon an 840 μm diameter tantalum disk, which acts as the cathode.

The pump laser is a Nd:YAG laser (Neodymium-doped yttrium aluminium garnet,$\mathrm{Nd : Y_3Al_5O_12}$) with a wavelength of 1064 nm. The wavelength of the pulsed beam is then doubled to 532 nm, attenuated using a combination of waveplates, and arrives at the sample at a 45° angle. A variable electronically controlled time delay

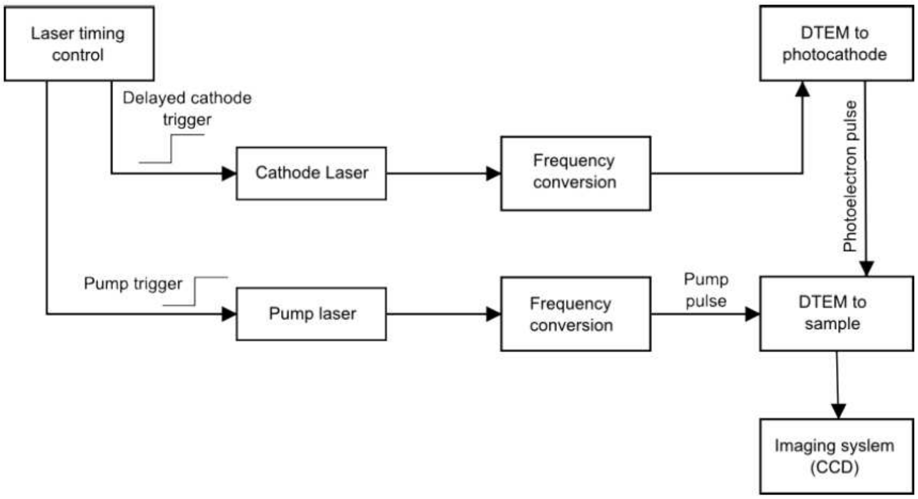

FIGURE 1–8: Schematic of the DTEM at LLNL.

between the two pulses ranges from 15 nanoseconds to arbitrarily long delays [41]. The image is then captured by state-of-the-art CCD coupled to a phosphor screen. The signal to noise for the detection of a single electron is 3-5.

A major challenge with the single shot technique is optimizing the electron pulse's brightness which is a limiting factor for the overall spatial resolution of the TEM. Brightness is defined as

$$B = \frac{Ne}{(\pi r^2)(\pi \alpha^2)\Delta t}, \tag{1.1}$$

where N is the number of electrons per pulse, e is the electronic charge, r is the electron beam radius, Δt is the duration of the pulse and α is the local convergence angle which is a measure of the lateral spatial coherence of the pulse [29]. The brightness is greatly improved through optimization of the initial laser spot profile, but maintaining the brightness as it travels down the column is challenging.

In the DTEM, the photoemission current is maximized but spatial coherence is lost to allow the condenser lens to accept much wider electron beams. To avoid blocking the beam with the cathode laser mirror, an additional lens was added before the first condenser. This allowed the beam to pass thorough the 1 mm diameter hole in the mirror and into the condenser with minimal aberrations. The improved coupling of the photoemitted beam into the first condenser lens improved the beam current by a factor of 20.

Coulomb interactions in the beam will affect its trajectory, resulting in loss of resolution. This effect is called stochastic blurring. In certain locations along the column, such as the sample position and the back focal plane, high electron density is unavoidable. The Coulomb repulsion worsens with high density pulses and longer propagation times, so stochastic blurring cannot be completely eliminated. A balance must be found between these blurring effects and electron dose conditions (time-resolution and bunch charge) to optimize the instrument operating conditions.

Fig. 1–9 shows the resolution limitation of the DTEM operating in single shot mode. The sample shown is composed of alternating layers of gold and carbon with spacings of 20 and 30nm. This is more than an order of magnitude better than the previous single-shot instruments [46]. Despite the DTEM's improvements, chromatic aberrations and unavoidable electron-electron repulsion in the pulse still limit the spatial resolution of the instrument [47]. In the third image, which was produced from a single 30 ns electron pulse, it is difficult to distinguish the 20nm layer spacing. Also, it is only possible to take one time resolved image per experiment. In order to build up a time series, multiple experiments must be performed at the same laser conditions on different sample areas. Inconsistencies in the sample must be avoided as much as possible since they are very detrimental to the results.

The greatest limitation of the DTEM is its temporal resolution. However, it can achieve a resolution of 15 ns, which is four orders of magnitude higher than using

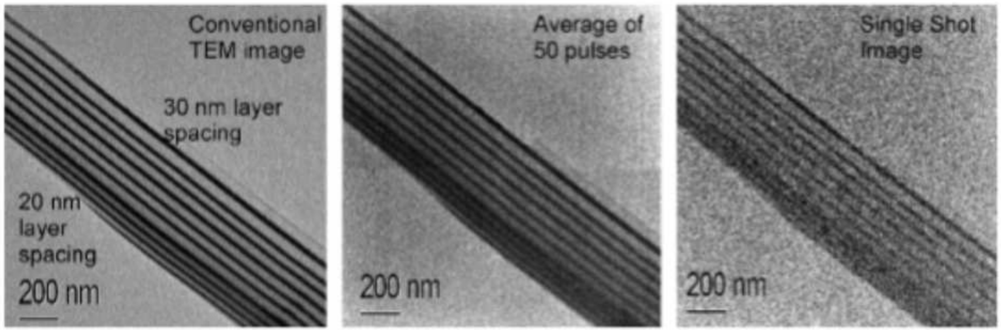

Figure 1–9: Spatial resolution limit for DTEM. Reprinted with permission from [3]. Copyright 2006, American Institute of Physics.

standard fast camera readout approaches. The resolution is sufficient to for many studies including catalytic reactions, crystallization and dislocation dynamics.

1.5 Thesis Goals

The remainder of this thesis outlines the application of DTEM technology to the study of laser induced, explosive crystallization of thin films of amorphous Germanium. Recent images taken by the DTEM at Lawrence Livermore National Laboratory (LLNL) are presented which illuminate new features of the time resolved microstructure of a-Ge during explosive crystallization. Thermal modelling techniques are applied to estimate the time dependent temperature profile. This information is then used to support conclusions about the crystallization dynamics of crystallization in three distinct morphological zones observed in the film. The results showcase the unique capabilities of the DTEM as a powerful tool for the study of irreversible dynamics in the structure of materials, as we are able to address many of the outstanding issues and overturn several earlier conclusions about these dynamics.

CHAPTER 2

Explosive Crystallization

Crystallization of amorphous semiconductor thin films has been a subject of intense experimental and theoretical investigation. From the perspective of fundamental science, the interest is due primarily to the rich physics involved in the process and its sensitivity to a number parameters (e.g. the film substrate temperature, film thickness, material parameters including heat capacity and thermal conductivity, the heat deposition rate used to crystallize the film). Crystallization under different conditions leads to different (final) film morphologies; the system provides a good example of pattern formation arising from growth instabilities. From the practical perspective, the research activity is due primarily to the applications of such films in modern electronics [48, 49] where laser or electron beam crystallization of amorphous semiconductor films has been exploited for the fabrication of solar cells, flat panel displays and IR detectors.

Amorphous semiconductor films are only metastable, and will spontaneously undergo a transition to the lower free energy crystalline state over a range of temperatures below the crystalline melting temperature (T_{mc}). An essential feature of this crystallization is the latent heat released at the crystallization front, which is significant; the latent heat (L) for the amorphous-crystalline (a-c) transformation divided by the specific heat capacity (C_p) is $L/C_p \sim 450$ K in Ge and ~ 420 K in Si. Over certain substrate temperature ranges the heat released can be sufficient to fuel a self-sustained crystallization front that propagates for distances a large as several centimeters once it is initiated (e.g. with laser or electron beam heating). Due to the 'autocatalyzed' nature of the crystallization, and since the process is accompanied by release of heat, sound and light emission it has been termed 'explosive crystallization' (EC). EC is a phenomenon common to amorphous semiconductors and some metals and is characterized by the rapid advancement of the crystallizing front away from the optical, thermal or mechanical source responsible for its initiation [50].

In this chapter we first review previous experimental studies of explosively crystallized a-Ge thin films [5,6,46] and provide a broad outline of the ideas and concepts that have provided some understanding of the process. We then present our recently obtained DTEM images of explosive crystallization in a-Ge that were taken on the instrument developed at Lawrence Livermore National Laboratory in Livermore, CA. This microscope was used in single-shot mode to generate images on a-Ge films during laser induced crystallization with unprecedented (nanometer-nanosecond) spatio-temporal resolution.

The spatio-temporal resolution in these DTEM studies was sufficient to reveal several important time dependent properties of the crystallization, such as nucleation and growth rate. With this information, the mechanism of crystallization is identified which helps to explain the morphology of the resulting structure.

2.1 Explosive Crystallization Overview

Geiler *et al.* distinguishes between four possible growth mechanisms that drive EC. In the case of an amorphous crystalline (a-c) transition that occurs completely in the solid state, there are two possible growth mechanisms. The growth can be governed by bulk-induced nucleation which occurs randomly in the film, this mode of EC is termed explosive solid-phase nucleation (ESPN). On the other hand if the crystal structure grows with an orientation corresponding to the substrate on which the film lies, the growth is termed explosive solid phase epitaxy (ESPE). EC can also occur via a mediating liquid zone between the amorphous and crystalline regions (a-l-c). The random nucleation and epitaxial growth are termed explosive liquid phase nucleation (ELPN) and explosive liquid phase epitaxy (ELPE), respectively. Fig. 2–1 illustrates the four different explosive crystallization processes.

To understand this liquid mode of crystallization, we consider a free energy diagram for germanium as a function of temperature (Fig. 2–2) as estimated in the calorimetric studies of Donovan *et. al.* [51]. The glass transition temperature, T_{ma}, and the crystallization temperature, T_{mc} are indicated. Melt mediated explosive crystallization (ELPN, ELPE) can occur when temperatures in the region of the crystallization front are within this range. Sharma *et. al.* describe ELPE using model called 'double duplex crytallization' (Fig. 2–3). A first order phase-transition in a-Ge occurs at $T_{ma} \sim 0.8\ T_{mc}$. This phase transition is described as being equivalent to 'melting' (rather than a glass transition), and produces an under-cooled meta-stable liquid. This results a rapidly growing crystalline phase. Thus, two co-propagaing phase boundaries, amorphous-liquid and liquid-crystal, can produce very high crystallization front speeds measured to be above 1 m/s. This is substantially more rapid than the corresponding solid phase growth (ESPN, ESPE) [52], which can occur at temperatures below T_{ma}. It is also important to note that although the a-l transformation is endothermic, the overall amorphous to liquid to crystalline process

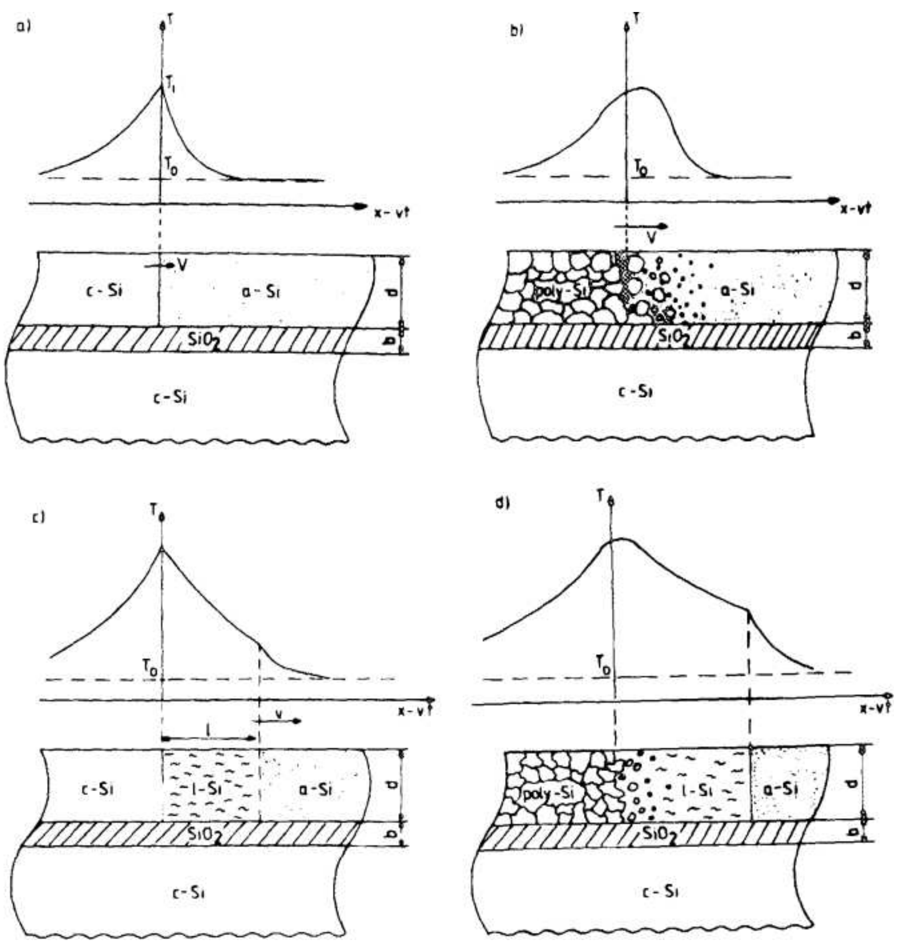

FIGURE 2–1: Schematics of the four different types of lateral explosive crystallization. a. ESPE, b. ESPN, c. ELPE and d. ELPN. Reprinted with permission from [4]. Copyright 1986, American Institute of Physics.

is exothermic, and this heat release is what drives further crystallization away from the initiation source.

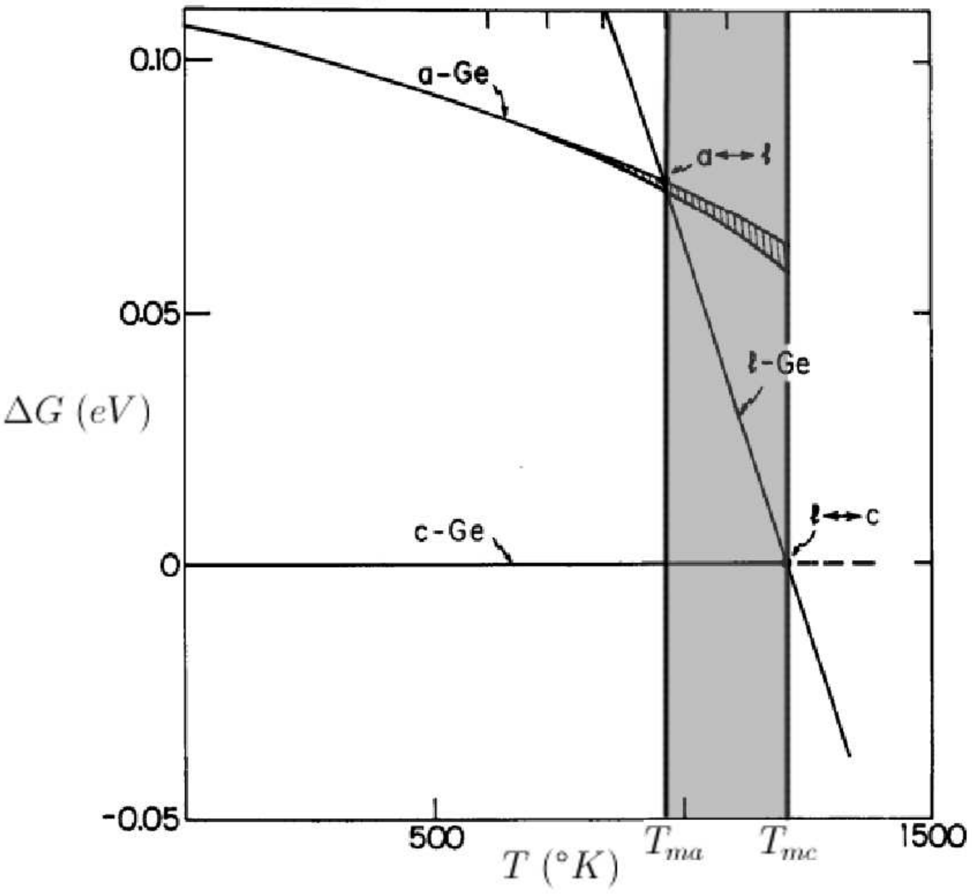

FIGURE 2–2: Free energy diagram for Ge in the amorphous (a-Ge) and liquid (l-Ge) phases given relative to the crystalline phase (c-Ge). The highlighted region shows where ELPE and ELPN may occur.

2.2 Experimental Work

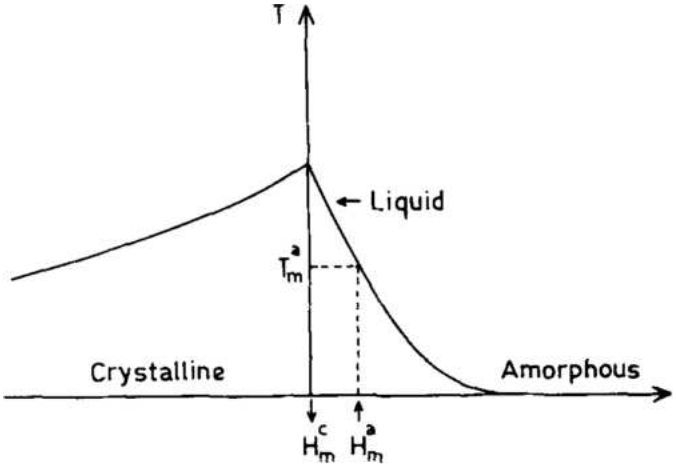

FIGURE 2–3: Schematic of the double duplex model. This explains the mechanism of the dendrite growth proposed in Sharma et. al. Reprinted with permission from [5]. Copyright 1984, American Institute of Physics

To study the solid state amorphous-crystalline transition, including ESPN and ESPE, various techniques have been used to initiate the process. These include thermal heating using a hot plate [53], pulsed laser heating [54] and others. Observations are made both *in situ* using optical techniques and *post mortem* by electron microscope. SEM images obtained by Koba *et. al.* are used to measure the interdependence of thickness and temperature in supporting propagation of the EC front [53]. Marine *et. al.* demonstrate a technique called the transient grating method, which uses the interference of two coherent light beams to observe heating and crystallization. The results reveal the crystallization time for both solid state and liquid mediated crystallization at nanosecond time resolution [54].

Experimental efforts to study the amorphous-liquid-crystalline transition have used many different techniques for observing the process. Electrical conductance, reflectance, transmittance thermal emission can all be measured in a time resolved manner to infer the structural dynamics of ELPE and ELPN [48,55,56]. For example reflectivity measurements have been used to determine interface velocity. In this way, it was shown that ELPE is the preferred process in amorphous silicon when EC is initiated by a Nd:glass laser [4,57]. In addition, Raman spectroscopy of reflected light has be used to calculate change in grain size as a function of laser pulse energy [58].

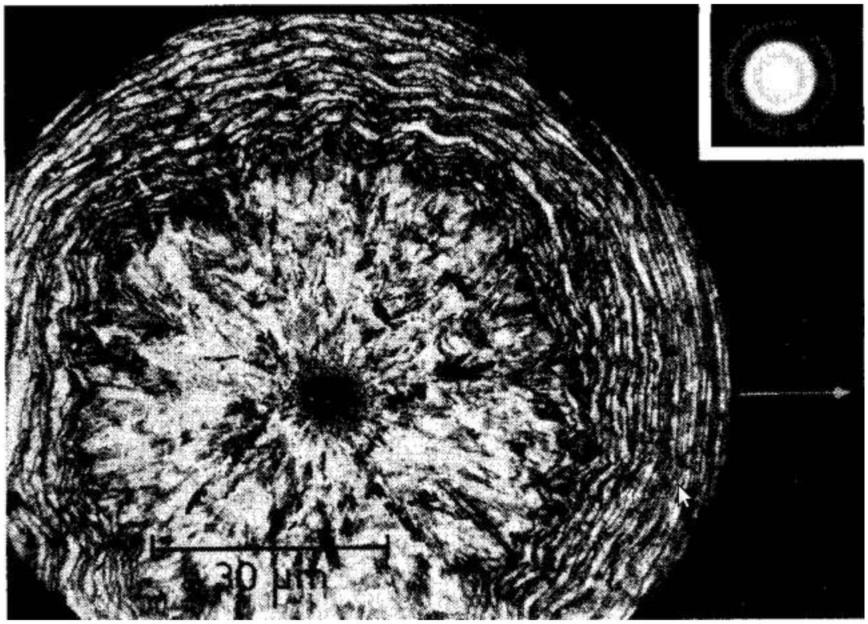

FIGURE 2–4: Explosive crystallization in an unsupported a-Ge film. Reprinted with permission from [5]. Copyright 1984, American Institute of Physics.

Although they produce time resolved results, these optical, electrical and thermal techniques cannot be used to directly observe the microstructure of the film. However, electron microscope images are able to resolve local structure *post mortem* [59–62]. A 1983 paper by Sharma *et. al.* [5] provides an example of basic analysis of EC in a-Ge without using time dependent instrumentation. An electron beam induced EC on unsupported a-Ge films, 200 nm thick. To prevent melting or vaporizing of the film, the beam current is kept at a low level. However the heat released from crystallization of the central region causes EC in the film. The results are shown in Fig. 2–4. The crystallization occurs in three distinct zones: The central region is filled with small crystallites, 10 ± 1 nm in diameter. This polycrystalline region extends out to a radial distance that matches the size of the electron beam (10 μm). Outside this boundary, radially oriented crystals, extend out to 30 μm. These single crystals are called dendrites due to their branching shape, and grow well beyond the illuminated region. Finally, the edges of the crystallized zone consists of alternating polycrystalline and dendritic rings. It is suggested that the periodicity of this pattern decreases with distance from the centre of the illuminated region.

In order to understand this behaviour, a thermodynamic analysis of the system was performed. It reveals that the approximate temperature in the film was 750K within a circle of radius 55-60 μm. The area around the central region reaches temperatures of above 1000K due to the heat of crystallization release in the polycrystalline zone.

The dendritic growth is ascribed to the aforementioned duplex model (Fig. 2–3, and the spiral shaped crystal mode that appears outside the dendritic area is attributed to a steep temperature gradient. This gradient would cause the polycrystalline growth to point inwards. The melt region outside this polycrystalline band remains stationary allowing single crystal growth which causes a steep temperature gradient to repeat the process.

This work provides important insights into the EC phenomenon in this geometry. In particular, the authors conclude that the input of energy required to crystallize the film outside the illuminated region comes from the heat of crystallization and not the electron-beam heat source. In addition, a mechanism for the dendrite growth involving liquid phase crystallization rather than a solid state transformation is proposed. However, the mechanisms cannot be determined confidently without a temporally resolved technique to view the time evolution of the EC process.

An early attempt at DTEM imaging of EC is presented in a 1985 paper by Bostanjoglo and Endurschat. Unsupported a-Ge films of thickness 60 to 80 nm are mounted in a transmission electron microscope modified to take time resolved (<4ns) images. The pulse used to induce crystallization was provided by a Nd-YAG pulsed laser with a pulse duration of 20 ns and a pulse width of 65 μm [46].

EC is observed in the film, shown in Fig. 2–5. The crystallization occurs in steps similar to those seen in Sharma's work. The central polycrystalline zone formed with all the crystallites having diamond structure and growing simultaneously at a speed of 9 ± 3 m/s about 40 ns after the incident pulse. The outer crystals grow in the radial direction at a much higher speed of 20 m/s about 100 ns later. These growth speeds can be used to identify the mode of crystallization.

If the heat source does not heat the film past the amorphous melting temperature $T < T_{ma}$, then the crystallization proceeds in the solid state at a velocity given by the Arrhenius law,

$$v_g \propto \exp\left(\frac{-E}{k_b T}\right), \tag{2.1}$$

where E is the activation energy of crystallization, k_b is the Boltzmann constant and T is the temperature of the film [46].

If the temperature is greater than the amorphous melting point but less than the crystalline melting point, $T_{ma} < T < T_{mc}$, the film enters a super-cooled liquid phase. The nucleation rate will be a relaxation type,

$$I \propto 1 - \exp\left(\frac{-t}{t_r}\right), \tag{2.2}$$

where t_r is the relaxation time which depends on the circumstances of nucleation.

It follows that assuming a diffuse plane phase boundary and spherical nuclei, one can obtain the growth rate,

$$v_g = 2af\left[1 - \exp\left(\frac{-H_c(T_{mc} - T)}{nk_bTT_{mc}}\right)\right]\exp\left(\frac{-\Delta G_a}{k_bT}\right), \tag{2.3}$$

where a is the nearest neighbour distance in the amorphous phase, f is the Debye frequency, H_c is the enthalpy of melting from the crystal phase, ΔG_a is the enthalpy of atomic diffusion in the amorphous phase and n is the density of nucleation sites.

For dendritic growth, growth velocity depends on the peak width. There exists a maximum velocity for supercooled liquid crystallization,

$$v_{g_{max}} = \frac{k_a(T_{mc} - T)^2}{8\sigma_{lc}T_{mc}}, \tag{2.4}$$

[46]

where k_a is the thermal conductivity of the amorphous phase and σ_{lc} is the interfacial energy between the liquid and crystalline regions [46].

A thermodynamic analysis based on measured values for Eq. 2.3 and Eq. 2.4, reveals upper and lower bounds on the growth velocity between 4 and 80 m/s. The delay and faster growth rate observed in the large outer crystals is attributed to the temperature rising above T_{ma} after some time by thermal diffusion and liberated latent heat, supporting the double-duplex model proposed by Sharma for the ELPE growth.

A follow up paper by the same author in 1987 provides improved images of the process (Fig. 2–5). Smooth crystallization front was observed as the dendrites grew outwards. The author asserts that this is explained by the Gibbs Thompson effect, which states that the growth speed of small crystallites melt at a lower temperature than the bulk liquid. Any protrusion will melt more readily than the rest of the

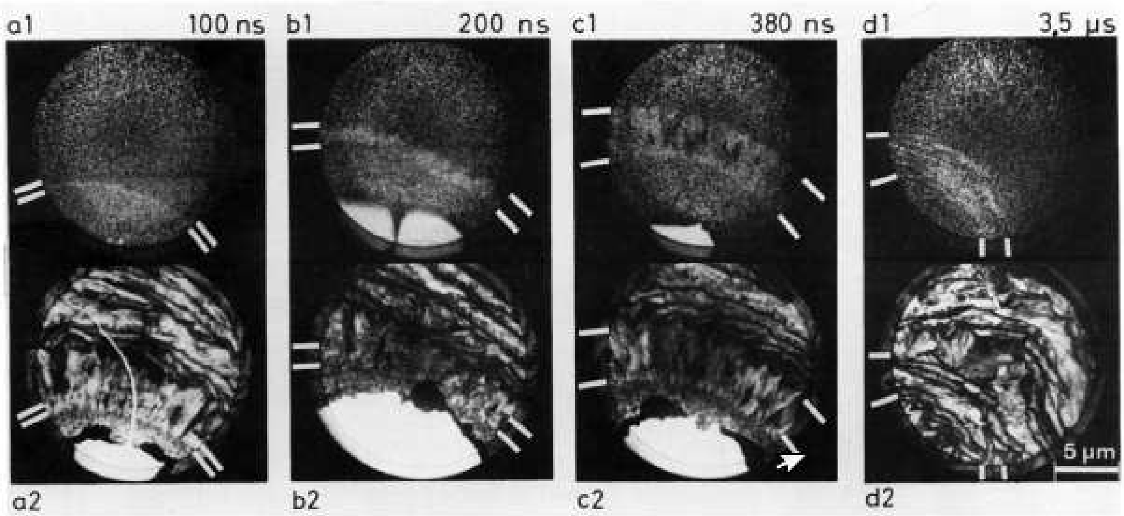

FIGURE 2–5: TEM images of intermediate stages of the explosive crystallization (top) alongside post mortem structure (bottom). Note the smooth crystallization front of the dendrites in the 200 ns and 380 ns image. Reprinted with permission from [6]. Copyright 1987, Elsevier B.V.

front which should keep growth front smooth [6]. These results, as well as the others mentioned earlier in this chapter, will be used as a basis of understanding for the modern experiments performed at LLNL.

2.3 Theoretical Work

Various models and simulations have been developed for the study of EC. Heat transport simulations, as well as atomistic simulations, of the direct a-c phase transition have been used to calculate the position, roughness and configuration of the amorphous-crystalline interface [63, 64]. These show periodic oscillations in front velocity [63], which are compared to a Mullins Sekerka type instability [65, 66],as described later in this chapter. Molecular dynamics simulations have also been done for liquid mediated EC. This method can calculate the interface temperature and speed as well as properties that would be difficult to observe, such as the width of the liquid layer [67]. Analytical theoretical treatments have been developed in parallel with these simulations [68–70].

A paper by J.S. Langer [65] presents a straightforward diffusion model for the temperature across a liquid-solid phase boundary. Let $u = \frac{T - T_m}{L/C_p}$ be a dimensionless diffusion parameter. Here, L is the latent heat of solidification T is the temperature and T_m is the melting point of the material.

Consider the continuity equation across the boundary as well as the steady state diffusion equation,

$$v_n = \alpha \left[\beta(\nabla u)_{solid} - (\nabla u)_{liquid}\right] \cdot \mathbf{n} \tag{2.5}$$

$$\nabla^2 u + \frac{2}{l_d}\frac{du}{dz} = 0 \tag{2.6}$$

where $\beta = \frac{(\alpha C_p)_{liquid}}{(\alpha C_p)_{solid}}$ and using a frame of reference moving at the interface velocity which we define as the z direction.

The boundary of the problem is subject to the Gibbs-Thompson effect, which states that small crystals in a liquid melt at a lower temperature than the bulk. This translates to undercooling at the boundary depending on its curvature, κ.

$$u_{interface} = -d_0 \kappa, \tag{2.7}$$

where the capillary length, $d_0 = \frac{\gamma T_m C_p}{H_c^2}$, is a function of the surface tension between the crystal and liquid phases, γ, and the other thermal properties of the crystal.

The solution of Eq. 2.5 assuming a flat interface,$\kappa = 0$, at $z = 0$, is

$$u = \begin{cases} \exp\left(\frac{-2z}{l_d}\right) - 1 & z \geq 0(\text{liquid}) \\ 0 & z \leq 0(\text{solid}) \end{cases},$$

Now, to analyze the stability of this system, define, $\zeta(x,t)$, the parametrized curve along the phase boundary. Assuming that the phase boundary moves much slower than the diffusion field, an approximate solution is given by solving Eq. 2.5 subject to Eq. 2.7 time independently, and then using the continuity equation to find an expression for $\frac{d\zeta}{dt}$.

Consider a small periodic perturbation in the interface,

$$\zeta(x,t) = \hat{\zeta}_k \exp(i\mathbf{k}\cdot\mathbf{x} + \omega_k t), \tag{2.8}$$

where $\mathbf{k}$ is perpendicular to the interface velocity and ω_k is called the amplification rate whose sign determines the stability of the interface. This perturbation adds the following terms to Section 2.3,

$$u = \begin{cases} \exp\left(\frac{-2z}{l_d}\right) - 1 + \hat{u}'_k \exp(i\mathbf{k}\cdot\mathbf{x} - q'z + \omega_k t) & \text{liquid} \\ \hat{u}_k \exp(i\mathbf{k}\cdot\mathbf{x} - qz + \omega_k t) & \text{solid} \end{cases},$$

where q and q' are given as functions of the wavevector, k. The details of the analysis can be found in [65] but the relevant result is given by the k dependence of the amplification rate,

$$\omega_k \simeq kv\left[1 - \frac{1}{2}(1+\beta)d_0 l_d k^2\right], \tag{2.9}$$

which is approximately valid in the limit that $kl_d \gg 1$. The wavenumber k_s where ω_k vanishes is the neutral stability point,

$$\lambda_s = \frac{2\pi}{k_s} = 2\pi\sqrt{(1+\beta)/2)l_d d_0} \simeq 2\pi\sqrt{l_d d_0}. \tag{2.10}$$

The rightmost expression of Eq. 2.10 is valid for $\beta \ll 1$. The maximum instability occurs at $k_s\sqrt{3}$ and patterns which emerge from this instability will initially have a characteristic size of order λ_s.

These considerations will be vital for the discussion of recent DTEM results outlined in Chapter 4 of this thesis.

CHAPTER 3

Theory and Modeling

DYNAMIC transmission electron microscopy can reveal in significant detail the microstructural evolution during the complex and extremely rapid nanosecond laser-induced crystallization of an amorphous semiconductor film, as shown in the previous chapter. Interpreting these images with the goal of explaining the growth mechanisms is further aided by an understanding of the time dependent temperature distribution in the sample. Since the DTEM provides accurate data for the distribution of the distinct crystallized zones and the speed and direction of crystal growth, these results also facilitate a temperature calculation based on thermal diffusion of the laser deposited energy and the exothermic crystallization front using a phenomenological approach. In this chapter the finite element algorithm developed to model the temperature profile in the film is described and results on the temperature evolution at the crystallization front through zone II are presented. This approach has the advantage of being a fully 2D calculation, allowing for angular asymmetry in the source terms and boundary conditions as necessary.

3.1 Thermal Modeling

A simple model is constructed to estimate the time dependent temperature profile of the film. The simplest model for 2D heat flow in a thin film is given by [71].

$$\frac{\partial u(x,y,t)}{\partial t} = \alpha \Delta u(x,y,t) + f(x,y,t), \tag{3.1}$$

where $u(x,y,t)$ is the temperature of the film at 2D postition, (x,y), and time, t. The source term, $f(x,y,t)$ is the rate at which the temperature changes at a point in time in units of [TemperatureDifference]/[Time]. The thermal diffusivity of the material is given by,

$$\alpha = \frac{k}{\rho C_p}, \tag{3.2}$$

where k is the thermal conductivity, ρ is the mass density and C_p is the specific heat at constant pressure. α is given in units of [Distance]^2/[Time]. This quantity can be used to calculate the diffusion length, l_d, which characterizes how far heat will propagate in the substance after a given time,

$$l_d = 2\sqrt{\alpha t}, \tag{3.3}$$

or

$$l_d = \frac{2\alpha}{v_n}, \tag{3.4}$$

where v is the directional derivative of the temperature by time in the **n** direction. This quantity can be used for comparing crystal nucleation and growth rates with the speed of the temperature front. An algorithm for finding solutions to Eq. 3.1 is discussed here.

3.1.1 2D Heat Diffusion

Consider the 2D heat equation on the domain, $\Omega \in \Re^2$, and its polygonal boundary Γ. Let $\Gamma_N := \Gamma \setminus \Gamma_D$, where Γ_D is the region where a solution must be set at specific values (Dirichlet) and Γ_N is the region where this holds for the first derivative (Neumann).

$$\begin{aligned} \frac{\partial u}{\partial t} &= \Delta u + f \qquad && \text{in } \Omega \times [0, \tau] \\ u &= u_d && \text{on } \Gamma_D \\ \frac{\partial u}{\partial n} &= g && \text{on } \Gamma_N \end{aligned} \tag{3.5}$$

3.1.2 Weak formulation

Where, $u(x, y, t)$ is the variable to be solved and $f(x, y, t)$ is the inhomogeneous term or applied heat. $u_D(t)$ is the fixed value of u on the boundary defined by the Dirichlet condition. g is the value of the directional derivative of u pointed in the normal direction, $\mathbf{n}$, defined by the Neumann condition.

For simplicity, let us assume Dirichlet conditions, that is to say $g \equiv 0$. We will now discretize the time dependence of the problem. We first partition the time interval into n subintervals, $[t_0 = 0, t_1], [t_1 = t_2], \ldots, [t_{n-1}, t_n = \tau]$. Define, $u_i = u(x, y, t_i)$, and apply the following scheme to Eq. 3.5.

$$(1 - dt\Delta)u_n = dtf_n + u_{n-1} \tag{3.6}$$

This is known as an implicit Euler scheme. Now, after integrating both sides over the domain, Ω, a test function, $v(x, y)$, is applied to both sides.

$$\int_\Omega u_n v dx - dt \int_\Omega \Delta u_n v dx = dt \int_\Omega f_n v dx + \int_\Omega u_{n-1} v dx \tag{3.7}$$

This is called the weak formulation of the boundary problem. The solution to this equation (called the weak solution) may not be an analytic function but will satisfy the above equation. The weak solution can be proved to exist using the Lax-Milgram lemma [72]. Finally, both sides are integrated by parts to explicitly apply the boundary conditions.

$$\int_\Omega u_n v dx + dt \int_\Omega \nabla u_n \cdot \nabla v dx = dt \left(\int_\Omega f_n v dx + \int_{\Gamma_D} g_n v ds \right) + \int_\Omega u_{n-1} v dx \quad (3.8)$$

3.1.3 Discretization

The problem will be reduced to a linear matrix equation. This will be implemented using a Galerkin method where u_n and v_n are replaced U_n and V_n which exist in a N-dimensional dimensional subspace, S, of the original function space.

$$\int_\Omega U_n V dx + dt \int_\Omega \nabla U_n \cdot \nabla V dx = dt \left(\int_\Omega f_n V dx + \int_{\Gamma_D} g_n V ds \right) + \int_\Omega U_{n-1} V dx \quad (3.9)$$

Now S will have a finite number of basis functions η_k and

$$U_n = \sum_{k \in I} u_{nk} \eta_k \quad (3.10)$$

$$V_n = \sum_{k \in I} v_{nk} \eta_k \quad (3.11)$$

where $I = [1, N]$. Applying Eq. 3.10 and Eq. 3.11 to Eq. 3.8,

$$\int_\Omega U_n \eta_j dx + dt \int_\Omega \nabla U_n \cdot \nabla \eta_j dx = dt \left(\int_\Omega f_n \eta_j dx + \int_{\Gamma_D} g_n \eta_j ds \right) + \int_\Omega U_{n-1} \eta_j dx. \quad (3.12)$$

Finally, the problem may be written in the form,

$$(dtA + B)U_n = dtf_n + BU_{n-1} \quad (3.13)$$

where,

$$A_{jk} = \int_{\Omega} \nabla \eta_j \cdot \nabla \ \eta_k dx \tag{3.14}$$

$$B_{jk} = \int_{\omega} \eta_j \eta_k dx \tag{3.15}$$

These are known as the Stiffness and Mass matrices respectively due to the analogous system of a restoring force (ie. Hookes law).

3.1.4 Constructing the Stiffness and Mass Matrices

Supposing that the domain Ω has a polygonal boundary, it is trivial to prove that there exists a set of triangles and quadrilaterals, $\mathcal{T}$, that covers Ω and whose intersection is zero [73]. Let $\mathcal{N}$ be the set of N nodes that comprise the vertices of the triangles in $\mathcal{T}$. The basis functions η_k may now be chosen to be delta functions corresponding to these nodes,

$$\eta_j(x_k, y_k) = \delta_{jk} \qquad j, k = 1, ..., N \tag{3.16}$$

Now, consider a single element, $T \in \mathcal{T}$, who only has three vertices,

$$\eta_j(x_k, y_k) = \delta_{jk} \qquad j, k = 1, 2, 3 \tag{3.17}$$

one can show that,

$$\eta_j(x, y) = \det \begin{pmatrix} 1 & x & y \\ 1 & x_{j+1} & y_{j+1} \\ 1 & x_{j+2} & y_{j+2} \end{pmatrix} \Bigg/ \det \begin{pmatrix} 1 & x_j & y_j \\ 1 & x_{j+1} & y_{j+1} \\ 1 & x_{j+2} & y_{j+2} \end{pmatrix} \tag{3.18}$$

and taking the gradient,

$$\nabla \eta_j(x, y) = \frac{1}{2|T|} \det \begin{pmatrix} y_{j+1} - y_{j+2} \\ x_{j+2} - x_{j+1} \end{pmatrix}, \tag{3.19}$$

where the area of a triangle, T is simply given by half the following determinant,

$$2|T| = \det \begin{pmatrix} x_2 - x_1 & x_3 - x_1 \\ y_2 - y_1 & y_3 - y_1 \end{pmatrix}. \tag{3.20}$$

Using this result, the stiffness matrix may now be assembled,

$$\int_T \nabla\eta_j \cdot \nabla\eta_k dx = \frac{1}{4|T|} \det \begin{pmatrix} y_{j+1} - y_{j+2} & x_{j+2} - x_{j+1} \end{pmatrix} \begin{pmatrix} y_{k+1} - y_{k+2} \\ x_{k+2} - x_{k-1} \end{pmatrix}. \tag{3.21}$$

Similarly, using the same identity (Eq. 3.17), the mass matrix is calculated.

$$\int_T \eta_j \eta_k dx = \frac{1}{24} \det \begin{pmatrix} x_2 - x_1 & x_3 - x_1 \\ x_2 - y_1 & y_3 - y_1 \end{pmatrix} \begin{pmatrix} 2 & 1 & 1 \\ 1 & 2 & 1 \\ 1 & 1 & 2 \end{pmatrix} \tag{3.22}$$

Lastly, consider the source term on the right hand side of the equation

$$\int_T f\eta_j dx \approx \frac{1}{6} \det \begin{pmatrix} x_2 - x_1 & x_3 - x_1 \\ x_2 - y_1 & y_3 - y_1 \end{pmatrix} f(x_S, y_S) \tag{3.23}$$

$$b_j = \sum_{T \in \mathcal{T}} \int_T f\eta_j dx \tag{3.24}$$

3.2 The Source Terms and Geometry

The parameters and dimensions of the DTEM geometry are 300μm ×300μm × 100nm a-Ge film supported by 40 nm of SiO. The thermal properties of the film are given in 3–1. The diffusion length for 10 μs (Eq. 3.3) is $l_d = 16\mu$m. So the temperature will not diffuse far enough to approach the boundary, thus we can assume simple Dirichlet boundary conditions where the film edges are held at room temperature.

For zone I, the thermal behaviour is extremely non-trivial. The initial pulse will certainly cause the a-Ge temperature to pass T$_{ma}$ and melt the film. If one calculates the temperature increase and naively neglects the phase transition that will occur, the temperature in zone I will reach nearly 2000 K. Of course, the actual temperatures will be much lower due to the different reflectivity and heat capacity of liquid germanium. Near the zone I boundary, however, the pump pulse imparts nearly a 10th of this energy. One must assume that somewhere in the illuminated region the temperature is enough to melt the film but not heat it past the crystalline melting temperature (1200K). This will ensure an area composed of undercooled melted film. Due to the metastable nature of the undercooled liquid germanium, the liquid will crystallize very quickly releasing exothermic energy into the film. This is the largest source of heat evolution in the film on the microsecond time scale. Since the thermal diffusion is slow, we assume the temperature in zone 1 is constant near the amorphous melting temperature, and phenomenologically model the source term based on the observed behaviour in zone II. The underlying temperature profile outside of zone I is initially set using the energy imparted from the excitation pulse. The Gaussian shape of the pulse causes the initial temperature profile outside of zone 1 to be shaped as a Gaussian tail.

For zone II and three, we have a travelling source term moving at $v_g = 8$ m/s and $v_g = 1$ m/s respectively starting at $t_{i_{z2}} = 0$ ns and ending at $t_{f_{z2}} = 10000$ ns. The dendritic crystallization front is discretized into a $\Delta_r = 50$ nm band which

Property	**Value**	**Source**
Density	5.0 ± 0.3 g/cm^3	[5]
Thermal Conductivity	130 ± 20 mW/cm^{3}K	[74]
Specific Heat	1.6 J/cm^{3}K	[75]
Heat of Crystallization $a \to c$	800 J/cm^3	[75]
Reflectivity (532 nm)	.51 ± .01	[76]
Absorption Length (532 nm)	2×10^5 cm^{-1}	[77]

TABLE 3–1: Physical Properties of amorphous Germanium.

moves at v_g starting from r_{z1} releasing the Latent heat $\Delta t = 5$ ns at a time.

$$f_{z2}(x,y,t) = \frac{L}{Cp\Delta t} h(t_{i_{z2}} - t) h(t - t_{f_{z2}}) h(r_{z1} + v_g(t - t_{i_{z2}})) - r) h(r - (r_{z1} + v_g(t - t_{i_{z2}}) + \Delta r)) \tag{3.25}$$

The small lengths required for this term require a very high spatial sampling which makes computation times impractical. Thus a grid with varying element sizes is used (Fig. 3–1).

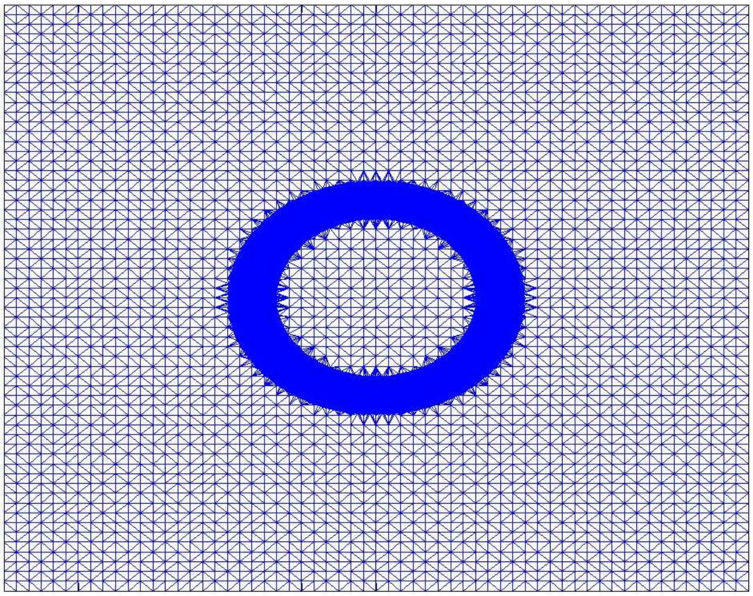

FIGURE 3–1: Triangulation of the grid used with $r_{z1} = 45$ highlighting the area of interest. Grid spacing is ten times finer in this region.

CHAPTER 4

Results and Discussion

4.1 Recent DTEM Results

The following section outlines measurements we performed with the state-of-the-art DTEM at LLNL. Crystallization in a 110nm a-Ge film supported by 40nm of SiO was observed. The a-Ge was deposited by e-beam evaporation onto commercially available 40 nm SiO films supported by 300-mesh copper grids. The amorphous nature of the Ge films was confirmed by x-ray diffraction and electron diffraction. After laser illumination with sufficient fluence, the film crystallizes into three morphologically distinct zones, denoted Zone I, II and III which are polycrystalline, dendritic, and spiral, respectively. These features correspond to those reported in Sharma et al. and Bostanjoglo et al.

4.1.1 Zone I

The features of Zone I as well as a discussion of the nucleation and growth kinetics are discussed at length in Nikolova, Stern et al. [78] For this DTEM experiment, the incident laser fluence was 128 mJ/cm^2, and the probe delay was set between 20 and 300ns.

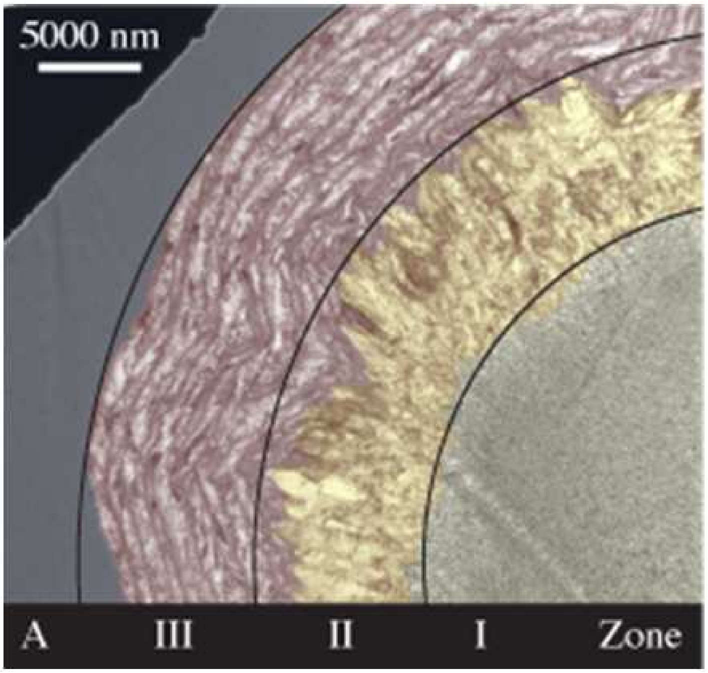

FIGURE 4–1: Post mortem image of the a-Ge Film. Zone I, bordered in red, is polycrystalline. Zone II, bordered in blue, consists of radial dendrites. Zone III, bordered in green, contains the alternating spiral bands.

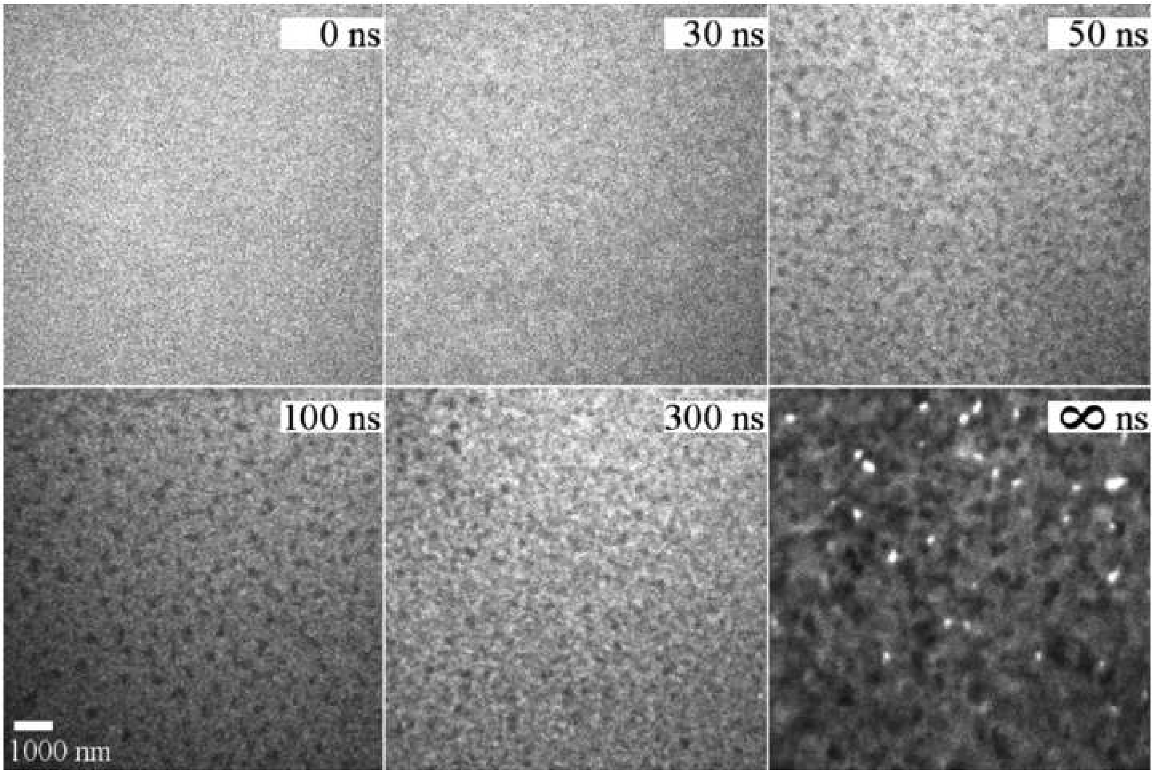

FIGURE 4–2: Time series of the nanocrystalline region.

A sample of the resulting images, from before pump (0 ns) to post mortem (∞ ns) are shown in Fig. 4–2. Near the center of the zone ($r < \sim 20\ \mu m$), where the temperature was highest, the size of the randomly nucleated crystal grains was measured as a function of time. The crystallization is initiated before 20 ns, which is consistent with prior results using optical techniques [79], and the contrast of the images darkens with increasing time delay until 50 ns. After this point the grain size does not increase significantly. Dark spots correspond to the growth of newly nucleated crystals and white spots are due to pores formed due to densification of the material or anisotropic growth and coalescence of grains similar to a previously reported crystallization behavior [5].

The grain size evolution retrieved from these images are shown in Fig. 4–3. The in-plane diameter of 100 crystals was measured, and the mean size was used for the result. The error bars in Fig. 4–3 are taken from the statistical variation the grain size since it is much higher than the image resolution (10 nm). The initial increase in grain size is linear. However, for time delays greater than 50 ns the increase in grain size is parabolic. From the data we can extract an estimate for the time for crystallization of 55 ns.

The nucleation rate was determined by simply counting the crystals in a 1 μm^2 area at each time step. The number of crystals increased dramatically for 40 ns and then decreased dramatically after than 60 ns, suggesting that complete crystallization occurs within 50-60 ns. The maximum nucleation rate is estimated at $1.6\times10^{22}\text{cm}^{-3}\text{s}^{-1}$, which is unsurprisingly high given the rapid crystallization and fine grain size.

Assuming the crystallization rate follows an Arrhenius relationship with the temperature (Eq. 2.1), we can estimate the temperature needed to fully crystallize the film in 55 ns. Using the activation energy (3 eV) and prefactor from Blum *et. al.* [80], we arrive at a temperature of 1700 K, well above the melting temperature. However, complete melting was not observed. A second estimate of the initial temperature rise can be made based on the pump pulse energies. Partial melting occurs at 195 mJ/cm^2 and complete melting at 220 mJ/cm^2. A calculation for 1D heat diffusion in the film was made that took into account the heat of fusion for the amorphous, crystalline change. Roughly, the temperature rise for a 128 mJ/cm^2 pulse should be between 800 and 1050K, corresponding to activation barriers between 1.4 to 1.9 eV. These temperatures and heating rates are much higher than those quoted in Blum *et. al.*

[80], which suggests additional mechanisms at higher temperatures or a temperature dependent activation barrier, which seems constant at lower temperatures.

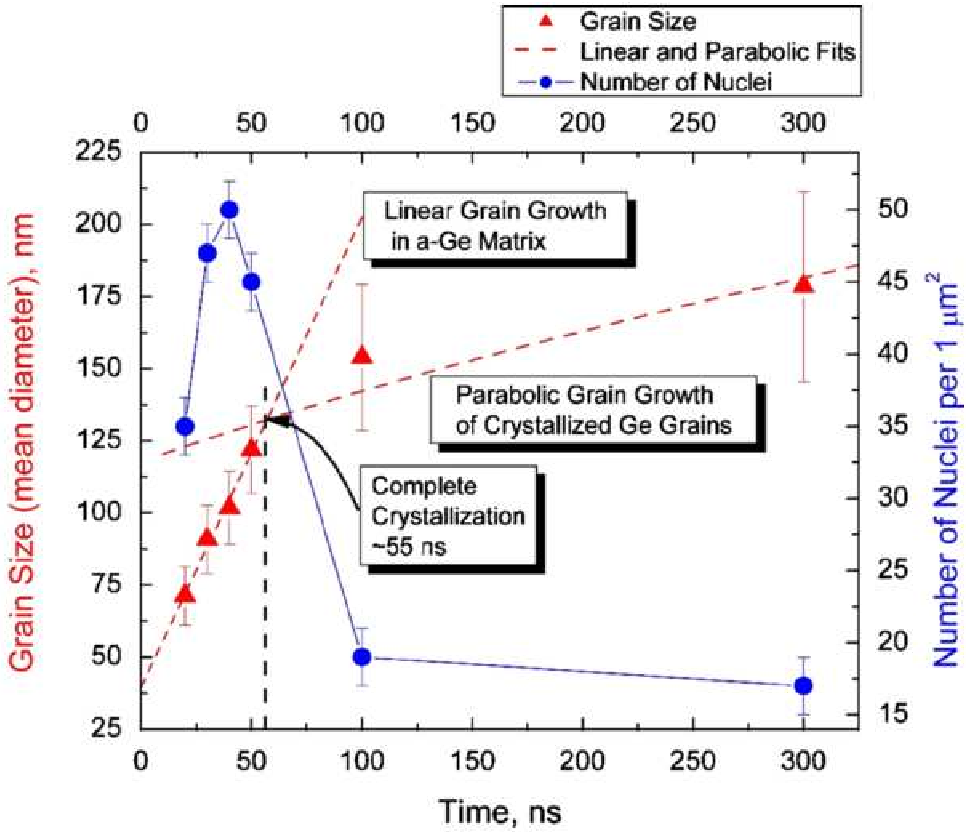

FIGURE 4–3: Nucleation and growth values for the central polycrystalline region.

4.1.2 Zone II

The data presented for Zones II and III are from a second DTEM experiment at LLNL, also discussed in Nikolova, Stern *et. al.*, Nature Materials, 2012 (Submitted). The pump laser fluence was 110 mJ/cm^2 with a 1/e^2 value of 100 μm. The Zone I/II boundary is between 45 and 50 nm which matches the 1/e^2 radius of the pulse. Fig. 4–4 and Fig. 4–5 are false coloured to show the difference between the *in situ* and the *post mortem* images. We observed that the dendrites start forming at 275

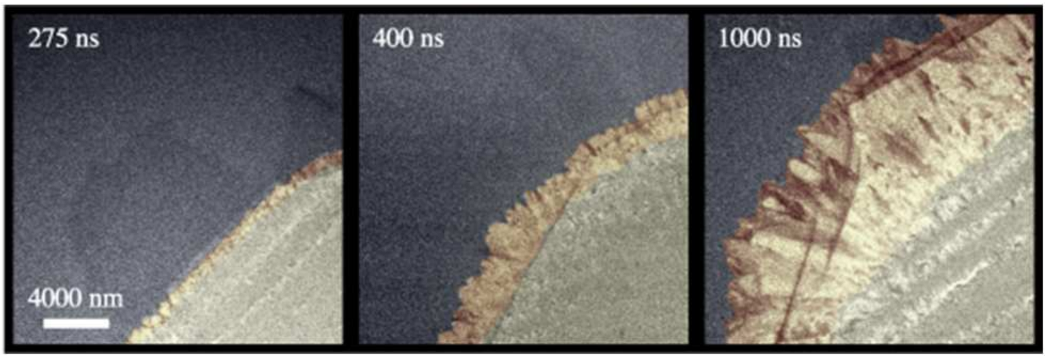

FIGURE 4–4: Time resolved, false colour images of the crystallization front at 275 ns, 400 ns and 100 ns.

ns and continue growing to 1300 ns. Many images accumulated over many specimen positions in this range of delay times suggests that the growth velocity is 8 ± 2 m/s and final dendrite size is 10 μm. In Fig. 4–4 it is clear that as the dendrites grow the number of branches decrease and each individual branch is becomes larger. The same images also show that the crystallization front roughens as it grows, not seen in the Bostanjoglo results.

4.1.3 Zone III

The outermost region contains alternating bands of nanocrystals and dendrites beginning at 55 μm. The crystallinity of each band was confirmed by electron diffraction. We observed the period of oscillation between bands to be 0.5-2.0 μm and the the outer edge varies greatly between samples. The nanocrystalline grain size is near 20 nm and the orientation of the dendrites is tilted azimuthally. Lastly, the dendritic growth direction is indicated in Fig. 4–5. This figure was produced by false colouring and superimposing the time resolved and *post mortem* images. The blue areas show structures that have already formed by 7500 ns after exposure and the red areas show structures that formed afterwards. The circle indicates position of growth front at 7500 ns.

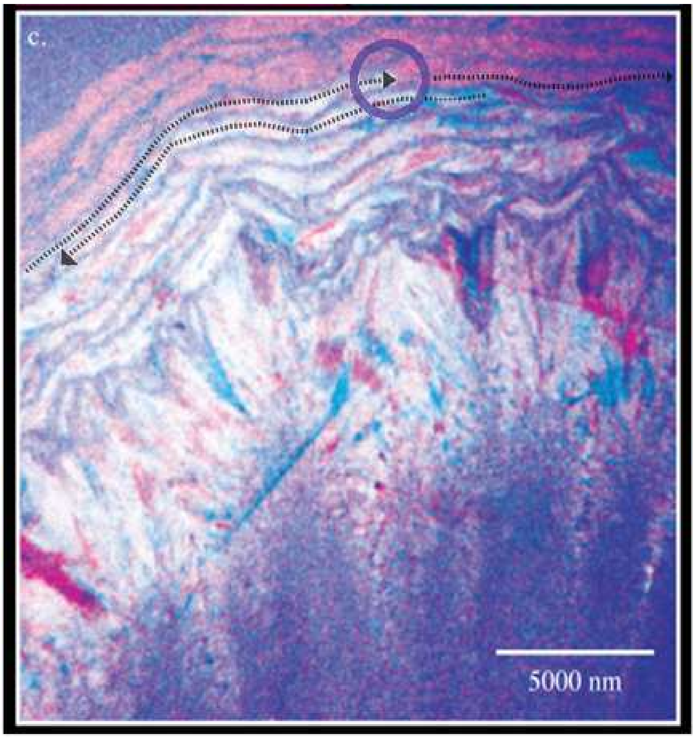

Figure 4–5: Difference between time resolved and post mortem images for the 7500 ns run; azimuthal growth indicated schematically. The circle indicates position of growth front 7500 ns after exposure.

4.2 Modeling Results

The results of the modelling are shown in Fig. 4–6. The striking result from this graph is the decrease in temperature in zone II as the dendrites grow and the levelling off of temperature in zone III.

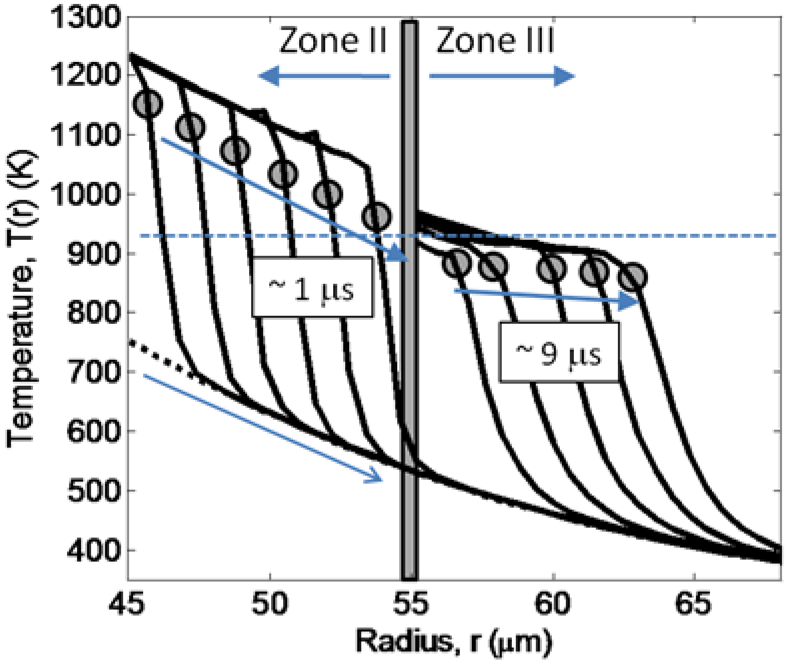

FIGURE 4–6: Plot of the calculated radial temperature profile in zones II and III. Circles indicate the temperature at the crystallization front. Note that the front temperature decreases throughout zone II and stays relatively constant in zone III.

4.3 Discussion

The crystallization through zone II observed in the DTEM images is clearly governed by the heat evolving laterally in the film. However, it can be shown that the thermal diffusion of the laser deposited energy in a-Ge is too slow to be a factor in the subsequent crystallization dynamics. For a-Ge, the diffusion length on microsecond timescales, given by Eq. 3.3, is only 3 microns, or more than an order of magnitude smaller than the distance between the centre of the pulse and the edges of the completed crystalline structure. Thus, it is clear that the energy from the pump pulse only initiates the crystallization and provides the temperature profile on which the crystallization evolves. The heat flow that drives the crystallization front is dominated by the exothermic heat of crystallization released at the crystallization front, diffusing over a short distance into the cooler surrounding amorphous material. In addition, the thermal energy released in the polycrystalline region does not transfer into the surrounding matter, until crystallization occurs at the zone boundary. Since the boundary is found to be very close to the 1/e^2 edge of the pulse, the radial temperature profile in Zone II will - initially - have the shape of a Gaussian tail before any crystallization occurs. The model also reveals that if the crystallization was taking place away from this 1/e^2 edge, the effect would not be the same.

Where the nanocrystalline region indicates a nucleation dominated mechanism, as seen in Fig. 4–2. On the contrary, the surrounding radially oriented crystals indicate a growth dominated mechanism. Time resolved images reveal protrusions that begin to appear on the initially flat growth front. Notably, they become increasingly large as the crystallization front travels outward. Previous studies suggest that the Gibbs Thompson effect should keep growth front smooth [6]. However, this behaviour can be understood as a result of Mullins-Sekerka type instability, as described in Section 2.3, which occurs due to localized temperature perturbations. Growth anisotropies can be attributed to the uneven temperature profile since the radius of the dendrite tips is proportional to the growth rate Eq. 2.3. The computed temperature profile shows a drop in temperature through Zone II Fig. 4–6 This corresponds with the roughening of the growth front, as well as the abrupt change in growth mode.

The speed of the crystallization front in Zone II reveals information about the crystallization mechanism in this region. Using 1 m radii and the measured radial front velocity of 8 m/s, the temperature at the inner boundary of Zone II is 1160K. The 2D temperature model also predicts temperatures in this range for Zone II. This temperature is below T_{mc} and above T_{ma} which strongly suggests that the crystallization front through Zone II is not a direct crystalline-amorphous boundary, but is in fact copropagating crystalline-liquid and liquid-amorphous interfaces. This gives a qualitative understanding of the melt mediated growth in Zone II.

The improved spatial resolution of the modern DTEM reveals new information that requires a revisiting of several earlier conclusions on the crystallization dynamics. In the 1987 paper by Bostanjoglo et. al., it is proposed that there is a pause, once Zone II has completely crystallized, to allow the laser deposited heat to traverse the crystallized region. Also Sharma suggested that Zone III crystallization occurs at higher temperatures than Zone II. The new results show that this is not the case for two reasons. First, according to the time resolved results there is no pause in crystal growth between Zones II and III. Second, the time scales for lateral heat diffusion in the film do not match those of the dynamics observed with the DTEM. As previously mentioned, the initial pulse contributes only to the initial temperature profile. The subsequent behaviour is caused by the exothermically released heat of crystallization. Also, in Sharma, it was concluded that the mechanism for Zone III crystallization proceeds inward. The time resolved images clearly show that the Zone III front velocity is azimuthally directed, as seen in Fig. 4–5.

An alternate explanation for the growth mode in Zone III is supported by the newly acquired data. The radial velocity of growth in Zone III is at least an order of magnitude less than in Zone II and the temperature behaviour revealed in the model predict that the temperature will dip below the amorphous melting temperature. This would mean that the crystallization will proceed without the mediating melt layer, and that a direct amorphous-crystalline transition will occur. The periodic layers of azimuthally oriented grains and nanocrystals indicate an oscillatory instability. It is hypothesized in Chonjacka's thesis that this tangential growth is melt mediated and can only occur at temperatures near the amorphous melting point [81]. A more detailed discussion of the structural dynamics in Zone III is beyond the scope of this thesis. In order to be accurate, a complete treatment of the 2D temperature flow would have to be presented. The phenomenological approach is not possible due to the non-trivial behaviour of the growth front in this region. However, the novel results presented here have lead to a new understanding of the crystallization dynamics in both Zone II and III, dramatically demonstrating the efficacy of the DTEM for studying time dependent material processes.

4.4 Conclusions and Future Efforts

The TEM has developed into an extremely powerful instrument for the study of equilibrium systems in materials science. Recent efforts to adapt these microscopes for for high time resolution imaging in a pump-probe mode have demonstrated that it is possible to take advantage of the TEMs unique capacity to study dynamic systems as well. Explosive crystallization in germanium films was observed by TEM bringing new insights into the crystallization dynamics and mechanisms involved in the formation of three qualitatively distinct morphological zones. Previous experiments were not able to completely, or accurately, explain the evolution of these structures due to their failure to provide time resolved images of the entire crystallization process and due to limits in spatial resolution. Combining, the state-of-the-art DTEM, capable of observing microstructural evolution at nm and ns spatial resolutions, with 2D thermal modeling, it is possible to produce novel conclusions about the structural evolution of explosive crystallization in a-Ge. Time resolved images of Zone II indicate a melt mediated crystallization mode evidenced by the rapid crystallization front velocity. In addition, Mullins-Sekerka like instability was observed, in the form of increasing roughness in the dendrites as they grow radially outward. The sudden transition to the oscillating Zone III morphology was seen to be a result of temperatures decreasing below a threshold temperature at the Zone II boundary, initiating a growth mode dominated by solid state crystallization.

The outlook for expansion of DTEM technology is promising. In the near future, an upgrade, called 'movie-mode', will allow multiple time resolved images of a single sample. A beam shifter will be installed to allow a train of electron pulses to be sent to the sample with various time delays. A high powered lens will rapidly redirect the electron beam to scan a grid on the CCD such that multiple images can be obtained at different time delays within a single experiment. This will allow tracking of individual structures as they evolve.

This thesis promoted the untapped potential for TEM technology in the study of non-equilibrium material processes. Clearly, the analysis of *post mortem* images is not sufficient to determine the details of microstructural evolution. The DTEM is ideal for use in this thriving field of study. Conventional techniques are blind to sub microsecond timescales, where the DTEM is uniquely able to produce previously unseen results. Efforts to develop this technology have already proved fruitful.

References

[1] J. Nelayah et al., Nature Physics **3**, 348 (2007).

[2] W. E. King et al., Journal of Applied Physics **97**, 111101 (2005).

[3] T. LaGrange et al., Applied Physics Letters **89**, 044105 (2006).

[4] H.-D. Geiler, E. Glaser, G. Gotz, and M. Wagner, Journal of Applied Physics **59**, 3091 (1986).

[5] R. K. Sharma et al., Journal of Applied Physics **55**, 387 (1984).

[6] O. Bostanjoglo, R. Tornow, and W. Tornow, Ultramicroscopy **21**, 367 (1987).

[7] P. E. Batson, N. Dellby, and O. L. Krivanek, Nature **419**, 94 (2002).

[8] M. Tanase and A. K. Petford-Long, Microscopy research and technique **72**, 187 (2009).

[9] X. Tan, Z. Xu, and J. K. Shang, Materials Science and Engineering: A **314**, 157 (2001).

[10] R. M. Tromp and F. M. Ross, Annual Review of Materials Science **30**, 431 (2000).

[11] P. A. Crozier, R. Wang, and R. Sharma, Ultramicroscopy **108**, 1432 (2008).

[12] P. L. Gai, Topics in Catalysis **8**, 97 (1999).

[13] P. L. Gai, Microscopy and Microanalysis **8**, 21 (2002).

[14] J. F. Creemer et al., Ultramicroscopy **108**, 993 (2008).

[15] J. M. Grogan and H. H. Bau, Journal of Microelectromechanical Systems **19**, 885 (2010).

[16] L. D. Marks, O. L. Warren, A. M. Minor, and A. P. Merkle, MRS Bulletin **33**, 1168 (2011).

[17] A. Minor, E. Lilleodden, E. Stach, and J. Morris, Journal of Materials Research **19**, 176 (2004).

[18] S. H. Oh, M. Legros, D. Kiener, and G. Dehm, Nature materials **8**, 95 (2009).

[19] O. Warren et al., Materials Today **10**, 59 (2007).

[20] H. H. Rose, Science and Technology of Advanced Materials **9**, 014107 (2008).

[21] P. B. Hirsch, Proceedings of the Royal Society of London. Series A, Mathematical and Physical Sciences **371**, 160 (1980).

[22] P. B. Hirsch, R. W. Horne, and M. J. Whelan, Philosophical Magazine **1**, 677 (1956).

[23] D. A. Porter and K. E. Easterling, *Phase transformations in metals and alloys*, Chapman & Hall, 1992.

[24] A. M. Minor et al., Nature materials **5**, 697 (2006).

[25] O. Bostanjoglo, R. Elschner, Z. Mao, T. Nink, and M. Weingärtner, Ultramicroscopy **81**, 141 (2000).

[26] H. Domer and O. Bostanjoglo, Review of Scientific Instruments **74**, 4369 (2003).

[27] T. LaGrange et al., Ultramicroscopy **108**, 1441 (2008).

[28] V. A. Lobastov, R. Srinivasan, and A. H. Zewail, Proceedings of the National Academy of Sciences of the United States of America **102**, 7069 (2005).

[29] B. W. Reed et al., Microscopy and microanalysis : the official journal of Microscopy Society of America, Microbeam Analysis Society, Microscopical Society of Canada **15**, 272 (2009).

[30] K. U. A. Takaoka, Journal of Electron Microscopy **37**, 117 (1988).

[31] A. H. Zewail, Science (New York, N.Y.) **328**, 187 (2010).

[32] M. R. Armstrong et al., Ultramicroscopy **107**, 356 (2007).

[33] G. H. Campbell, T. LaGrange, J. S. Kim, B. W. Reed, and N. D. Browning, Journal of electron microscopy **59 Suppl 1**, S67 (2010).

[34] T. R. O. Bostanjoglo, Mikroskopie **32**, 190 (1976).

[35] F. Carbone et al., Chemical Physics Letters **468**, 107 (2009).

[36] F. Carbone, O.-H. Kwon, and A. H. Zewail, Science (New York, N.Y.) **325**, 181 (2009).

[37] D. J. Flannigan, P. C. Samartzis, A. Yurtsever, and A. H. Zewail, Nano letters **9**, 875 (2009).

[38] O.-H. Kwon, B. Barwick, H. S. Park, J. S. Baskin, and A. H. Zewail, Nano letters **8**, 3557 (2008).

[39] H. S. Park, J. S. Baskin, and A. H. Zewail, Nano letters **10**, 3796 (2010).

[40] B. Barwick, H. S. Park, O.-H. Kwon, J. S. Baskin, and A. H. Zewail, Science (New York, N.Y.) **322**, 1227 (2008).

[41] M. R. Armstrong, B. W. Reed, B. R. Torralva, and N. D. Browning, Applied Physics Letters **90**, 114101 (2007).

[42] B. Barwick, D. J. Flannigan, and A. H. Zewail, Nature **462**, 902 (2009).

[43] A. Yurtsever, R. M. van der Veen, and A. H. Zewail, Science (New York, N.Y.) **335**, 59 (2012).

[44] G. H. O. Bostanjoglo, physica status solidi (a) **73**, 95 (1982).

[45] M. R. Armstrong et al., Ultramicroscopy **107**, 356.

[46] O. Bostanjoglo and E. Endruschat, physica status solidi (a) **91**, 17 (1985).

[47] P. W. Hawkes et al., *Science of Microscopy*, Springer New York, New York, NY, 2007.

[48] M. Hatano, S. Moon, M. Lee, K. Suzuki, and C. P. Grigoropoulos, Journal of Applied Physics **87**, 36 (2000).

[49] Y.-C. Her, C.-W. Chen, and C.-L. Wu, Journal of Applied Physics **99**, 113512 (2006).

[50] C.-C. Kuo, W.-C. Yeh, J.-B. Chen, and J.-Y. Jeng, Thin Solid Films **515**, 1651 (2006).

[51] E. P. Donovan, F. Spaepen, D. Turnbull, J. M. Poate, and D. C. Jacobson, Journal of Applied Physics **57**, 1795 (1985).

[52] L. Csepregi, R. Küllen, J. Mayer, and T. Sigmon, Solid State Communications **21**, 1019 (1977).

[53] R. Koba, Applied Physics Letters **40**, 672 (1982).

[54] W. Marine and P. Mathiez, IEEE Journal of Quantum Electronics **22**, 1404 (1986).

[55] M. Hatano, S. Moon, M. Lee, K. Suzuki, and C. P. Grigoropoulos, Journal of Non-Crystalline Solids **266-269**, 654 (2000).

[56] C. Grigoropoulos, M. Rogers, S. Ko, a. Golovin, and B. Matkowsky, Physical Review B **73** (2006).

[57] G. Andrä, H.-D. Geiler, G. Götz, K. H. Heinig, and H. Woittennek, physica status solidi (a) **74**, 511 (1982).

[58] M. Mulato, Journal of Non-Crystalline Solids **227-230**, 930 (1998).

[59] C. Cesari, G. Nihoul, J. Marfaing, W. Marine, and B. Mutaftschiev, Journal of Applied Physics **57**, 5199 (1985).

[60] C. Césari, G. Nihoul, J. Marfaing, W. Marine, and B. Mutaftschiev, Surface Science **162**, 724 (1985).

[61] J. R. Parsons and C. W. Hoelke, Philosophical Magazine A **50**, 329 (1985).

[62] M. Lee, S. Moon, M. Hatano, K. Suzuki, and C. P. Grigoropoulos, Journal of Applied Physics **88**, 4994 (2000).

[63] V. A. Levin and A. S. Leibenzon, Combustion, Explosion, and Shock Waves **21**, 101 (1985).

[64] M. Posselt and a. Gabriel, Physical Review B **80**, 1 (2009).

[65] J. S. Langer, Reviews of Modern Physics **52**, 1 (1980).

[66] D. Kurtze, W. van Saarloos, and J. Weeks, Physical Review B **30**, 1398 (1984).

[67] E. Albenze, M. Thompson, and P. Clancy, Physical Review B **70**, 1 (2004).

[68] W. van Saarloos and J. Weeks, Physical Review Letters **51**, 1046 (1983).

[69] W. Van Saarloos and J. D. Weeks, Physica D: Nonlinear Phenomena **12**, 279 (1984).

[70] V. Shklovskij and V. Ostroushko, Physical review. B, Condensed matter **53**, 3095 (1996).

[71] M. Grimaldi, P. Baeri, and M. Malvezzi, Physical Review B **44**, 1546 (1991).

[72] J. Alberty, C. Carstensen, and S. A. Funken, Numerical Algorithms **20**, 117 (1999).

[73] P. Ciarlet, *The Finite Element Method for Elliptic Problems*, North-Holland, Amsterdam, 1978.

[74] P. Nath and K. Chopra, Physical Review B **10**, 3412 (1974).

[75] H. S. Chen, Journal of Applied Physics **40**, 4214 (1969).

[76] J. Prins, *Physics of non-crystalline solids proceedings of the international conference, Delft, July, 1964.*, North-Holland Pub. Co.;;Interscience Publishers, Amsterdam ;New York, 1965.

[77] J. Stuke, Journal of Non-Crystalline Solids **4**, 1 (1970).

[78] L. Nikolova et al., Applied Physics Letters **97**, 203102 (2010).

[79] F. Heinricht and O. Bostanjoglo, Applied Surface Science **54**, 244 (1992).

[80] N. A. Blum and C. Feldman, Journal of Non-Crystalline Solids **22**, 29 (1976).

[81] A. Chojnacka, *Explosive Crystallization of Germanium Films: Kinetics and Morphologies*, PhD thesis, Cornell University, 2002.